HHS Public Access

Author manuscript

Cell Rep. Author manuscript; available in PMC 2024 July 11.

Published in final edited form as:

Cell Rep. 2024 June 25; 43(6): 114291. doi:10.1016/j.celrep.2024.114291.

A *cis*-regulatory module underlies retinal ganglion cell genesis and axonogenesis

Kamakshi Mehta[1,7], **Marwa Daghsni**[1,7], **Reza Raeisossadati**[6], **Zhongli Xu**[2], **Emily Davis**[1], **Abigail Naidich**[1], **Bingjie Wang**[1], **Shiyue Tao**[2], **Shaohua Pi**[1], **Wei Chen**[2], **Dennis Kostka**[3], **Silvia Liu**[4], **Jeffrey M. Gross**[6], **Takaaki Kuwajima**[1,5], **Issam Aldiri**[1,3,5,8,*]

[1]Department of Ophthalmology, University of Pittsburgh School of Medicine, Pittsburgh, PA 15213, USA

[2]Department of Pediatrics, University of Pittsburgh School of Medicine, Pittsburgh, PA 15213, USA

[3]Department of Computational & Systems Biology, University of Pittsburgh School of Medicine, Pittsburgh, PA 15213, USA

[4]Department of Pathology, University of Pittsburgh School of Medicine, Pittsburgh, PA 15213, USA

[5]Louis J. Fox Center for Vision Restoration, University of Pittsburgh School of Medicine, Pittsburgh, PA 15213, USA

[6]Department of Molecular Biosciences, The University of Texas at Austin, Austin, TX, USA

[7]These authors contributed equally

[8]Lead contact

SUMMARY

Atoh7 is transiently expressed in retinal progenitor cells (RPCs) and is required for retinal ganglion cell (RGC) differentiation. In humans, a deletion in a distal non-coding regulatory region upstream of ATOH7 is associated with optic nerve atrophy and blindness. Here, we functionally interrogate the significance of the Atoh7 regulatory landscape to retinogenesis in mice. Deletion of the Atoh7 enhancer structure leads to RGC deficiency, optic nerve hypoplasia, and retinal blood vascular abnormalities, phenocopying inactivation of Atoh7. Further, loss of the *Atoh7* remote enhancer impacts ipsilaterally projecting RGCs and disrupts proper axonal projections to the visual thalamus. Deletion of the Atoh7 remote enhancer is also associated with the dysregulation

*Correspondence: aldirii@pitt.edu.

AUTHOR CONTRIBUTIONS

Conceptualization, I.A., K.M., and M.D.; investigation, K.M., M.D., R.R., E.D., A.N., B.W., S.P., J.M.G., and T.K.; data curation, S.L.; visualization, K.M., M.D., E.D., and R.R.; formal analysis, Z.X., S.T., W.C., D.K., and S.L.; writing, I.A. and K.M.; supervision I.A., T.K., and J.G.M.

DECLARATION OF INTERESTS

The authors declare no competing interests.

SUPPLEMENTAL INFORMATION

Supplemental information can be found online at https://doi.org/10.1016/j.celrep.2024.114291.

of axonogenesis genes, including the derepression of the axon repulsive cue Robo3. Our data provide insights into how Atoh7 enhancer elements function to promote RGC development and optic nerve formation and highlight a key role of Atoh7 in the transcriptional control of axon guidance molecules.

Graphical Abstract

In brief

In this study, Mehta et al. dissect the roles of Atoh7 *cis*-regulatory elements during retinogenesis. They demonstrate that deleting the enhancer landscape upstream of Atoh7 phenocopies Atoh7 mutant mice histologically and transcriptionally. They also found that loss of the remote enhancer affects ipsilateral RGCs and their projections to the brain.

INTRODUCTION

Retinal development is achieved through sequential coordinated steps that ultimately lead to the generation of seven major cell types, born in a conserved order.[1,2] Initial retinal developmental events involve the expansion of the retinal progenitor cell (RPC) pool through multiple rounds of cell division before progenitors exit the cell cycle and give rise to six neuronal and one glial cell type.[1,3] Retinal ganglion cell (RGC) differentiation originates during embryonic stages as a result of an early wave of neurogenesis under the control of the retinal progenitor transcription factors. This leads to the expression of the basic-helix-

loop-helix (bHLH) transcription factor *Atoh7* in retinal precursors between embryonic day (E)11 and E14.5 in the mouse retina.[4–6] *Atoh7* is required for RGC differentiation in zebrafish, mice, and humans.[7–11] Additionally, murine retinae deficient of Atoh7 display persistence of the hyaloid vasculature, disruption of post-natal blood vessels, and abnormal electrophysiological responses.[12,13] Previous studies indicated that *Atoh7* triggers a genetic program that includes the expression of several transcription factors required for RGC terminal differentiation.[6,14,15]

How Atoh7 expression is controlled during retinogenesis has been under intensive investigation. A potential primary regulatory mechanism of gene expression underlies *cis*-regulatory elements, which govern transcriptional outputs spatially and temporally.[16,17] Earlier work has identified a highly conserved mouse *Atoh7 cis*-regulatory constituent (termed a proximal enhancer), 1.5 kb upstream of its transcription start site (TSS), which drives the expression of a reporter gene in a pattern similar to endogenous *Atoh7* in transgenic frogs.[18,19] In humans, a large deletion in a distal non-coding region upstream of ATOH7 is associated with nonsyndromic congenital retinal nonattachment (NCRNA) disorder, characterized by optic nerve atrophy and complete blindness. It was suggested that the missing DNA region acts as a remote regulatory element that governs Atoh7 expression through an as-yet unexplored mechanism.[20] This element (termed a remote enhancer) is conserved in mammals and matches the spatiotemporal expression of *Atoh7* in transgenic mice, further suggesting that it regulates Atoh7 and implying a functional similarity between mice and humans.[20] Subsequent human genetic studies identified mutations in the Atoh7 coding region that are associated with key features of NCRNA.[10,21] However, whereas the orthologous mouse deletion of the remote enhancer leads to a significant reduction in Atoh7 expression in the developing retina, it does not phenocopy NCRNA, and RGCs appear to be minimally affected in adult retina.[22] Thus, the functional relevance of the *Atoh7* enhancer landscape in mice and humans remains poorly understood, and a mouse model that recapitulates NCRNA disease is yet to be generated. This information is necessary for understanding the pathological manifestations of NCRNA and improving RGC generation paradigms from stem cells.

Here, we comprehensively investigated the requirement of the mouse Atoh7 enhancer landscape *in vivo*. We demonstrate that deletion of the entire *cis*-regulatory element upstream of Atoh7 leads to the loss of RGCs and the absence of the optic nerve, with structural, functional, and transcriptional abnormalities comparable to what is observed upon Atoh7 inactivation. We further show that disruption of the Atoh7 remote enhancer leads to transcriptional aberrations in axonogenesis genes and defects in RGC axon innervations to the visual centers in the brain. Our data provide insights into how Atoh7 enhancer elements function to promote RGC genesis and axonogenesis and uncover a key role of Atoh7 in the transcriptional control of axon guidance molecules that may include chromatin-based mechanisms.

RESULTS

Detailed mapping of the *cis*-regulatory signature dynamics near Atoh7 in the developing retina

We first comprehensively investigated the chromatin dynamics of *Atoh7 cis*-regulatory topology in mice using the assay for transposase-accessible chromatin with sequencing (ATAC-seq) and chromatin immunoprecipitation sequencing (ChIP-seq) analyses of 8 stages of murine retinal development.[23] The chromatin accessibility and enhancer signature defined an enhancer signal within 3 kb of the *Atoh7* TSS, corresponding to the previously characterized proximal enhancer.[18] A second, more pronounced, major putative regulatory region is located approximately 9 kb from *Atoh7* (distal/remote enhancer) and is associated with the occupancy of the active enhancer marks H3K27Ac, BRD4, and RNA polymerase II (RNAPII), and discernible with ATAC-seq peaks (Figure 1A). Interestingly, whereas the binding dynamics of BRD4 and RNAPII correlated well with the timing of Atoh7 expression, H3K4me3 and H3K27Ac deposition persisted in post-natal stages and show little evidence of decommissioning (Figure 1A). We also found that the Atoh7 locus accumulated the polycomb-mediated repressive mark H3K27me3 after E14.5 as Atoh7 expression subsided (Figure 1A). The reduction in H3K27me3 deposition in later post-natal stages may reflect the decline in the proportions of RGCs and RPCs as late-born cell-type genesis progresses in the post-natal developing retina.

To delineate the cell-type-specific accessibility pattern of *Atoh7* at E14.5, when Atoh7 expression peaks, we performed single-cell (sc)-ATAC-seq (103 Genomics). Our analysis revealed 9 clusters of cells spatially organized in a continuum-like pattern that mirrors the progression from proliferation to differentiation at E14.5, in agreement with previous data[24,25] (Figures 1B and S1; Table S1). We annotated cell cluster identity based on chromatin accessibility profiles associated with well-established retinal cell-type-specific markers and identified five major retinal cell populations known to be present at E14.5: RPCs, neurogenic precursor cells, RGCs, horizontal/amacrine cells, and cones (Figures 1B and S1; Table S1). Chromatin accessibility of Atoh7 and its enhancers was predominant in cell clusters underlying the transition from an RPC-like state to differentiation (Figures 1B–1D and S1). Specifically, an increase in *Atoh7* chromatin accessibility in areas corresponding to the proximal and distal (remote) enhancer regions was observed in retinal neurogenic precursor cells (cluster 4) and spanned differentiating cones and RGCs clusters (clusters 5 and 7, respectively) and then became less abundant in differentiated RGCs (cluster 8) (Figures 1B–1D and S1). The highly accessible open chromatin configuration of the Atoh7 enhancer in differentiating cones is interesting and in agreement with the suggested roles of Atoh7 in cone genesis.[26,27] To confirm these data, we integrated sc-ATAC-seq with sc-RNA-seq performed on wild-type (WT) E14.5 mouse retina using a recently developed method that employs imputed gene activity scores from sc-ATAC-seq data as the reference.[28,29] In line with our sc-ATAC-seq annotations, Atoh7 activities are highest in the neurogenic cluster, followed by the RGC and cone clusters (Figure S1; Table S1). Overall, the single-cell analyses corroborate the results of our bulk chromatin analyses, reflecting the pronounced transient expression of *Atoh7* in retinal precursor cells as they exit the cell cycle and differentiate into RGCs.[30]

Structural and functional defects in the retina upon loss of the Atoh7 enhancer landscape

To functionally test whether the mouse Atoh7 enhancer landscape is necessary for retinogenesis, we generated an enhancer knockout (KO) that spans its entire regulatory landscape (termed Atoh7-TEN: total retinal enhancer for Atoh7) using CRISPR-Cas9 (Figure 2A). Homozygous KO mice are viable and fertile, but gross morphological analyses of *Atoh7-TEN*$^{-/-}$ brains indicated hypoplasia of the optic nerve and chiasmata, signifying RGC deficiency (Figure 2B). To assess structural defects in the adult retina of *Atoh7-TEN*$^{-/-}$ mice, we carried out high-axial-resolution fiber-based visible-light optical coherence tomography (vis-OCT) imaging[31] on mutant animals and aged-matched controls (Figure 2C). We found that the optic nerve head was under-developed and, in many cases, was difficult to distinguish, while the nerve fibers were dramatically reduced and their morphology was abnormal (Figure 2C). Additionally, the retina and RGC layer thickness was significantly reduced (Figure S2; $n = 6$ mice for WT; 9 mice for *Atoh7-TEN*$^{-/-}$, $p < 0.0001$).

Loss of RGCs is also associated with defects in retinal blood vessels.[12,21,32] To determine whether the blood vasculature was affected in Atoh7-TEN mutant retina, we performed OCT angiography on adult WT and *Atoh7-TEN*$^{-/-}$ mice. We detected defects in the superficial vascular plexus, a network of large blood vessels proceeding radially from the optic nerve head to the periphery in a star-shaped manner (Figure 2C; $n = 6$ mice for WT; 9 mice for *Atoh7-TEN*$^{-/-}$).[33] Overall, OCT data underscore striking morphological defects in the primary blood vessels and in the patterns of the smaller capillaries, including neovascularization, abnormal tortuosity, lack of/multiple merging points for outlet, and/or sudden termination (Figures 2C and S2; Video S1, S2, and S3). We also detected evidence of retinal detachment and persistent fetal vasculature, a failure of the regression of the retinal embryonic vasculature in the post-natal retina, reminiscent of the human eye disease persistent hyperplastic primary vitreous, and a feature of NCRNA (Figures 2C and S2; Videos S1 and S2).[20,21,34] To examine the blood vasculature defects histologically, we performed immunostaining of the endothelial cell marker CD31 (PECAM1) on whole flat-mount adult retina from control and *Atoh7-TEN*$^{-/-}$ animals.[32,35] We observed loss of the superficial vascular plexus structure and defects in the blood capillary network branching, particularly in the peripheral retina, in agreement with data from Atoh7-deficient mice (Figure S2).[12,32]

To assess the consequences of disrupting the Atoh7 enhancer on the retinal electrophysiological activities, we performed electroretinogram experiments on age-matched adult mice from WT and Atoh7-TEN-deficient lines. Data underscore the loss of vision and a significant reduction in A and B waves ($n = 6$ mice/group, $p < 0.001$), indicating severe functional defects in photoreceptors and retinal interneuron responses, respectively (Figures 2D and S2).

Histological analysis of the retina using H&E staining revealed several structural defects in the *Atoh7-TEN*$^{-/-}$ mice, including reduced retina thickness, disruption of the laminar structure, the absence of the optic stalk, and ectopic blood vessels in the vitreous, all of which are reminiscent of loss of Atoh7 in the retina (Figure 2E). Taken together, we

conclude that the Atoh7 enhancer landscape is required for proper retina morphology and function.

The Atoh7 enhancer landscape is essential for RGC genesis and axonogenesis

The lack of the optic nerve and optic chiasm in the *Atoh7-TEN*$^{-/-}$ ice suggests a loss of RGCs. To test this, we performed immunolabeling of the RGC markers RBPMS, BRN3B (POU4F2), BRN3A (POU4F1), ISL1, TUBB3, and PAX6 on adult retina from WT and *Atoh7-TEN*$^{-/-}$ mice. The results indicated a strong reduction in the staining of those markers, underscoring a substantial decline in RGC numbers in the mutant retina (Figures 2E and S3). Indeed PAX6^{+} cells in the RGC layer were significantly reduced ($n = 3$ per group, $p < 0.001$; Figure S3). The residual presence of PAX6^{+} cells in the RGC layer likely represents displaced amacrine cells (Figure 2E).[7] We also examined the possible effect of Atoh7-TEN deficiency on different retinal cell types by immunostaining retinal sections from adult control and *Atoh7-TEN*$^{-/-}$ animals with cell-type-specific markers (Figure S3). We found that most cell types suffered from a significant reduction, consistent with a previous report.[36]

The reduction in RGC staining can be detected as early as in post-natal day (P)0 retina of the mutant mice, indicative of a developmental defect (Figure S3). To further delineate whether RGC differentiation is affected in the Atoh7-TEN-deficient mice, we performed immunolabeling of the RGC markers OC2, ISL1, TUBB3, and BRN3B (POU4F2) at E14.5, when RGC genesis peaks (Figure 3A). We observed a severe decrease in the RGC markers at this stage in *Atoh7-TEN*$^{-/-}$ retina compared to control (Figure 3A). To corroborate these results and elucidate the transcriptional programs impacted in E14.5 *Atoh7-TEN*$^{-/-}$ retinae, we performed bulk RNA-seq analysis and identified 1,571 downregulated and 370 upregulated transcripts ($n = 4$ for each genotype; >1.5-fold change; adjusted $p < 0.05$; Table S2). Atoh7 was among the most significantly downregulated genes (>90% reduction, adjusted $p < 0.05$), along with well-established regulators of RGC differentiation, including Isl1, Pou4f2, Eya2, and Myt1l (Figure 3B; Table S2). Significantly upregulated transcripts included genes such as the proneural bHLH factors Neurod1, Neurog2, and components of Notch signaling, all of which are known to be increased upon the loss of Atoh7 (Figure 3B).[37] Gene Ontology (GO) analysis using the database for annotation, visualization, and integrated discovery[38] revealed that downregulated and upregulated genes are significantly associated with functions related to nervous system development and neurogenesis (Figure 3C).

The above phenotypic and transcriptomic changes are consistent with the proposed role of Atoh7 in promoting RGC differentiation. To further evaluate this on a global level, we examined the degree of transcriptional overlap between the Atoh7-TEN deletion and the Atoh7 gene KO in the developing retina. Using RNA-seq data generated from *Atoh7*$^{-/-}$ retinae,[37] we defined 569 (84.5%) and 121 (50.6%) transcripts that were commonly downregulated and upregulated in Atoh7 gene KO, respectively (Figures 3D; Table S2). Overall, genes that are known to be transcriptional targets for Atoh7 were similarly impacted in both *Atoh7*$^{-/-}$ and *Atoh7-TEN*$^{-/-}$ retina. For instance, shared upregulated genes include factors such as Gadd45g, Bhlhe22, and Vxn (3110035E14Rik), while Hhip, Ebf3,

and Pou6f2 are among those that are commonly downregulated (Table S2). To further corroborate these results, we intersected the differentially expressed genes (DEGs) from our bulk RNA-seq analysis with the cell-type-specific DEGs previously identified in sc-RNA-seq performed on the developing retina from the Atoh7 gene KO.[37] Data indicate that RGC clusters are highly enrichmed with DEGs from our bulk RNA-seq, followed by cone clusters (Figure S3; Table S2). Taking these results together, we conclude that the Atoh7 enhancer landscape is required for proper RGC genesis, phenocopying inactivation of Atoh7 in mice and NCRNA in humans.

Transcriptomic analysis of the Atoh7 remote enhancer KO

Previously, it was shown that loss of the murine Atoh7 remote enhancer led to a significant reduction in Atoh7 expression.[22] However, the corresponding transcriptional changes in the developing retina of this mouse have not been investigated. Considering the apparent contrast between the robust decrease in Atoh7 expression and the lack of a strong phenotypic impact in the Atoh7 remote enhancer KO mice, we sought to investigate the transcriptome of the developing retina in this enhancer KO in detail. We used CRISPR-Cas9 to generate a mouse KO (termed Atoh7-REN hereafter) lacking the remote enhancer (Figure 4A). We found no obvious gross abnormalities in eye size or retina structure in adult mice carrying Atoh7-REN deletion, and immunolabeling of RGC markers indicated that RGCs were formed, recapitulating previously published results[22] (Figures 4B–4G). To elucidate possible molecular mechanisms, we assessed the transcriptional programs affected in the *Atoh7-REN*$^{-/-}$ retinae by carrying out bulk RNA-seq at E14.5 ($n = 3$ for each genotype; Figure 4H; Table S3). The analysis identified a total of 308 of differentially expressed transcripts, far less than what was observed in the *Atoh7-TEN*$^{-/-}$ retina, of which 153 were downregulated and 155 were upregulated (>1.5-fold change; adjusted $p < 0.05$; $n = 3$; Table S3). Compared to the near-complete loss of the Atoh7 transcript in *Atoh7-TEN*$^{-/-}$ retina (>99%; adjusted $p < 0.05$), Atoh7 expression was significantly reduced in the *Atoh7-REN*$^{-/-}$ retinae by 80% (Figures 4H and 4I; Table S3). However, contrary to the *Atoh7-TEN*$^{-/-}$ retinae, we found a mixed effect on the expression of the RGC gene regulatory network (GRN) in the Atoh7-REN-deficient retina (Figures 4H and 4I; Table S3). Aside from Atoh7, many of the known RGC regulatory transcription factors downstream of Atoh7 did not pass the 0.5-fold reduction threshold (e.g., Isl1, 0.37-fold reduction; Pou4f2, 0.39-fold reduction; adjusted $p < 0.05$, $n = 3$ for each genotype), while others were not significantly impacted (e.g., Pou4f1, adjusted $p = 0.87$; Table S3; Rbpms, adjusted $p = 0.34$; Figure 4I; Table S3). This is in far contrast to the robust fold reduction observed in Atoh7-TEN KO (0.83-, 0.81-, 0.80-, and 0.63-fold decreases for Isl1, Pou4f2, Pou4f1, and Rbpms, respectively; adjusted $p < 0.05$, $n = 3$; Figure 4I; Table S2). Globally, we found little overlap between the transcriptome of Atoh7 KO and *Atoh7-REN*$^{-/-}$ retinae. Only 12.5% of downregulated (84/670) and 9.2% (22/239) of upregulated transcripts were significantly changed in Atoh7 KOs, with the fold change of many of these genes generally less than what was observed in *Atoh7-TEN*$^{-/-}$ mice (Table S3). In conclusion, despite the robust reduction in Atoh7 expression in *Atoh7-REN*$^{-/-}$, the expression of key components of the GRN underlying RGC genesis does not seem to be critically sensitive to Atoh7 dosage perturbation, and RGC development managed to proceed with minimal interruption.

Cell-type-specific changes in Atoh7 expression in Atoh7-*REN*$^{-/-}$ retina

To delineate the underlying cell-type-specific transcriptional programs in the *Atoh7-REN*$^{-/-}$ retina, we carried out sc-RNA-seq analysis on retinae from WT and *Atoh7-REN*$^{-/-}$ mice at E14.5. We successfully identified 9 clusters organized into 5 major cell types: RPCs, neurogenic cells, cones, RGCs, and amacrine/horizontal cells, in agreement with published data[39] (Figure 4J; Table S3). Uniform manifold approximation and projection visualization indicated no major differences in the cluster composition between WT and Atoh7-REN-deficient retinae, and we found that the key members of the GRN associated with RGC development were expressed in the mutant retina, while Atoh7 was significantly downregulated, supporting our bulk RNA-seq data (Figures 4J–4M). Interestingly, we observed that the downregulation of the Atoh7 transcript was disproportional across cell types (Figures 4L and 4M). Whereas retinal precursor cells (neurogenic cells) maintained some level of Atoh7 expression, it was strongly reduced in differentiating RGCs and cones (Figures 4L and 4M).

Atoh7 is required for the proper binocular visual circuit formation

GO term analysis of the top transcriptionally downregulated genes (adjusted $p < 0.05$) in the Atoh7-REN-deficient retinae indicated the enrichment of pathways associated with axon development, guidance, and neuron projection (Figure 5D). Thus, we hypothesized that aspects of axon growth and/or guidance might be particularly affected in the *Atoh7-REN*$^{-/-}$ retina. To investigate this, we analyzed optic nerve innervations to the dorsal lateral geniculate nucleus (dLGN), a key relay center to convey visual information from RGCs to the visual cortex.[40] RGC axon terminals from contra- and ipsilateral eyes occupy non-overlapping domains of the dLGN, whereby small ipsilateral projections localized to the medial dLGN, while contralateral axons terminated in the distal areas.[41] Using well-characterized methods,[42–44] we performed anterograde axonal labeling using Alexa Fluor 488-conjugated cholera toxin subunit B (CTB 488) and Alexa Fluor 555-conjugated CTB (CTB 555) on P30 mice. These tracers were injected intravitreally into the left and right eye of WT and *Atoh7-REN*$^{-/-}$ mice, respectively. As expected, ipsilateral axons from WT animals formed bundles and projected to the medial dLGN (Figures 5A–5C). In *Atoh7-REN*$^{-/-}$ mice, the overall structure of the dLGN in the mutant mice appeared intact, and RGC axons managed to reach the dLGN (Figure 5A). Strikingly, however, ipsilateral axons vigorously defasciculated, and their axons inappropriately invaded contralateral-occupied terminals within the dLGN (Figures 5A and 5B; $n = 3$ for each genotype, $p < 0.05$). Thus, we conclude that Atoh7 is required for the proper establishment of the eye-specific retinogeniculate projection.

Atoh7 is associated with chromatin-regulated axon guidance cues

Analysis of RNA-seq data from the *Atoh7-REN*$^{-/-}$ retina at E14.5 suggests that several axonogenesis genes are dysregulated, including Ntn1, Nell2, Eph3a, and Eph4a ($n = 3$ for each genotype, adjusted $p < 0.05$; Table S3). Interestingly, one of the most upregulated genes in our RNA-seq dataset was Robo3, a non-canonical member of a family of receptors that acts to repel growing axons from inappropriate targets (8-fold increase, adjusted *p*

< 0.05; n = 3/group; Figure 5E).[45] The deregulation of Robo3 expression in *Atoh7-REN*$^{-/-}$ retina is selective, as the expression of the other family members Robo-1, -2, and -4 remained unchanged (n = 3 for each genotype; Figures 5E; Table S3). This was particularly interesting given that Robo3 is expressed at low levels in the WT retina, which warrants further investigation. We first corroborated these data by performing fluorescence *in situ* hybridization of Robo3 on E14.5 WT and *Atoh7-REN*$^{-/-}$ retina (Figure 5G). Importantly, using our sc-RNA-seq profiling, we discovered that the upregulation of Robo3 occurred mainly in the RGC lineage (Figure 5F). To test the impact of ectopic Robo3 on optic nerve pathfinding, we turned to zebrafish and generated a *5xUAS*:robo3b.1-p2A-tdTomatoCAXX transgenic line, where ectopic Robo3-expressing cells are labeled by membrane-bound Tomato. We then overexpressed robo3b.1 under the control of the *vsx2* regulatory element (*vsx2*:Gal4), which drives expression in RPCs.[46] To ensure that non-specific protein overexpression does not affect the optic nerve, we utilized *vsx2*:Gal4;*14xUAS*:Kaede, which expresses the benign Kaede protein in the same vsx2 domain as robo3b.1, as a control. At 5 days post-fertilization, all *vsx2*:Gal4;*14xUAS*:Kaede embryos showed normal optic nerve morphologies and pathfinding to the chiasm (Figure S4). In contrast, all *robo3b.1*-overexpressing embryos showed defects in optic nerve pathfinding (Figure S4). 4/9 of these were classified as severe, with axonal trajectories deviating substantially dorsally before redirecting ventromedially toward the optic chiasm (Figure S4), while the remaining 5/9 were milder in phenotype but still displayed this dorsal flexion of the optic nerve (Figure S4).

To investigate possible molecular mechanisms underlying Robo3 upregulation in the retina, we profiled the chromatin signature nearby the Robo3 locus and discovered that the Robo3 promoter is bivalently occupied by the active histone mark H3K4me3 and the repressive mark H3K27me3, the latter of which is catalyzed by the activities of the polycomb repressive complex (PRC2; Figure 5I).[47,48] Interestingly, the nearby family member Robo4 is devoid of such deposition, indicating a selective targeting of Robo3 by chromatin-mediated regulation (Figure 5I). We hypothesized that Robo3 is H3K27me3 repressed via a mechanism that, directly or indirectly, involves Atoh7. To address this, we queried transcriptomic data published on the murine developing retina deficient of Ezh2,[49] which is the catalytic subunit of the PRC2 and is required for H3K27me3 deposition.[50] We found that Robo3 is indeed significantly upregulated in the Ezh2 KO retina (n = 4 per group; 3-fold increase, adjusted $p < 0.0001$; Figure 5H).[49] We then tested whether the reduced expression of Atoh7 observed in *Atoh7-REN*$^{-/-}$ results in a concomitant reduction in H3K27me3 occupancy on the Robo3 promoter. We performed H3K27me3 ChIP-seq on the developing retina from WT and *Atoh7-REN*$^{-/-}$ retina at E14.5 and found no obvious differences in H3K27me3 enrichment on the Robo3 promoter between WT and *Atoh7-REN*$^{-/-}$ retinae (Figure 5J). We speculate that this result likely reflects the relatively small number of retinal cells showing Robo3 derepression in the *Atoh7-REN*$^{-/-}$ retina (Figure 5G). Whether the derepression of Robo3 in *Atoh7-REN*$^{-/-}$ is directly mediated by the loss of H3K27me3 acquisition remains unclear. Taken together, we conclude that the Atoh7 distal *cis*-regulatory element is required for proper expression of axonogenesis gene expression and transcriptionally regulates the H3K27me3-occupied Robo3.

ipRGCs are significantly affected in the Atoh7-REN KO

Analysis of the total ipsilateral axon density in the dLGN of *Atoh7-REN*$^{-/-}$ mice indicated a significant reduction in axon projection compared to *Atoh7-REN*$^{+/+}$ mice (Figure 5C, $n = 4$ per group; $p < 0.05$). Ipsilateral RGC (ipRGC) projections originate from a small population of RGCs that occupy the ventral retina.[43,51,52] Interestingly, Atoh7 is expressed in iRGCs at E15.5, and a recent work suggests a possible involvement of Atoh7 in the formation of ipRGCs.[53,54] We reasoned that differentiation of the ipRGCs is particularly impacted in *Atoh7-REN*$^{-/-}$ mice during retinogenesis. To test this hypothesis, we immunoassayed the developing retina from *Atoh7-REN*$^{-/-}$ and *Atoh7-REN*$^{+/+}$ embryos for Isl1/2 (pan-RGC marker) and Zic2, which is highly expressed in the peripheral ventral RGCs from E14.5 to E18.5 (Figure 6A).[52,55] We quantified the number of RGCs in the peripheral ventral temporal (VT; Zic2^{+}, Islet1/2^{+}) and dorsal temporal (DT; Islet1/2^{+}) retina of *Atoh7-REN*$^{-/-}$ and WT embryos at two time points, E14.5 and E17.5 (Figures 6B–6D and S4). When compared to control, we noted that E17.5 *Atoh7-REN*$^{-/-}$ retina showed a slight, but significant, decrease in the number of DT and VT Islet1/2^{+} cells ($n = 3$/group; $p < 0.05$), consistent with previously reported data[22] (Figures 6A–6C and S4). However, intriguingly, ipRGCs are more significantly reduced compared to contralateral RGCs in *Atoh7-REN*$^{-/-}$ embryos at E17.5 but not E14.5 ($n = 3$/group, Figures 6D and S4). To confirm these data, we crossed our *Atoh7-REN*$^{-/-}$ mice to the *Slc6a4:Cre; R26R*^{ZsGreen} mouse line, which specifically expresses ZsGreen under the control of the ipRGC-specific marker SERT (encoded by Slc6a4).[42,55] We found a significant reduction in ZsGreen^{+} cell number in *Atoh7-REN*$^{-/-}$ mice in comparison to control ($n = 5$/group, Figures 6E and 6F). Thus, our data indicate that the Atoh7 remote enhancer is particularly required for iRGC development.

Tissue-specific requirement of Atoh7 enhancer landscape

Enhancers function to drive gene expression in a specific spatiotemporal manner during organogenesis.[16] Outside the retina, *Atoh7* is post-natally expressed in the mouse and human cerebellum,[56] albeit at lower levels than in the retina, raising the interesting question of whether the regulatory activities of the Atoh7 enhancer elements in the cerebellum and the retina are functionally and structurally distinct. We first defined the *cis*-regulatory architecture in the cerebellum at P18, a time point of noticeable Atoh7 expression, by carrying out ChIP-seq analyses of the active chromatin marks H3K27Ac and H3K4me2 (Figure 7A). We observed high concordance of H3K27Ac and H3K4me2 enrichment nearby Atoh7 between the retina at E14.5 and the cerebellum at P18 (Figure 7B). To delineate the functional potential of the Atoh7 enhancer landscape on the cerebellar Atoh7 transcription, we performed bulk RNA-seq on the cerebellum at P18 from WT, *Atoh7-REN*$^{-/-}$, and *Atoh7-TEN*$^{-/-}$ mice. Remarkably, loss of the remote enhancer does not affect cerebellar Atoh7 expression ($n = 3$/group, adjusted $p > 0.05$), while Atoh7-TEN deficiency led to a ~50% reduction in the Atoh7 transcripts ($n = 3$/group, adjusted $p < 0.05$; Figure 7C; Table S4). Collectively, these data suggest that the requirement of the Atoh7 core *cis*-regulatory elements for its expression is highly tissue restricted.

DISCUSSION

Given the phenotypic similarity between NCRNA disorder and Atoh7 inactivation in mice, it was proposed that a *cis*-regulatory element that lies within a non-coding genomic deletion in NCRNA governs Atoh7 expression.[20] While this hypothesis awaits conclusive validation, two lines of evidence support its premises. First, the missing human genomic DNA fragment can recapitulate the spatial expression of Atoh7 in mice.[20] Second, cases of patients with NCRNA phenotypic manifestations carrying mutations in the coding region of Atoh7 have been reported.[9,10] As retinogenesis is conserved on the cellular and molecular level in humans and mice, it is reasonable to suggest that disruption of the corresponding murine non-coding region would phenocopy NCRNA. A preliminary prediction to this hypothesis is that, in addition to DNA sequence similarity, the analogous mouse Atoh7 genomic landscape would be conserved on the chromatin level, bearing the chromatin hallmarks of active enhancers. Indeed, combined with previous data, our comprehensive epigenomic profiling of the mouse developing retina defined such a putative regulatory region with precision, revealing that it is marked by an active enhancer signature with developmental dynamics that mirror the transient expression of Atoh7. Our integrated single-cell analysis further validated these results, showing a robust correlation between cell-type-specific Atoh7 chromatin accessibility dynamics and Atoh7 expression. Notably, the Atoh7 locus in mice and humans seems to accumulate the repressive histone mark H3K27me3 as Atoh7 expression declines, reflecting its poised transcriptional state in embryonic stem cells (Figure 1; data not shown). Whereas the presence of a bivalent domain (concurrent enrichment of H3K4me3 and H3K27me3) on the developmental genes in embryonic stem cells primes cells for their subsequent activation during lineage differentiation,[57] the biological significance of H3K27me3 deposition on Atoh7 in the developing retina is unknown. A compelling hypothesis is that it may prevent spurious activation of Atoh7 past the temporal window of RGC genesis. A recent study established a related paradigm whereby the polycomb-mediated repression of Foxp1, an early RPC transcription factor, is essential to restrict prolonged production of early-born retinal cell types.[58] However, conditional inactivation of Ezh2, the catalytic subunit of PRC2, does not lead to the upregulation of Atoh7 in E16 retina or the expansion of the RGC population.[49,59] Thus, the functional implication of H3K27me3 deposition on the Atoh7 promoter remains unclear.

The Atoh7 enhancer landscape contains two key regulatory regions, termed proximal and distal enhancers.[18,20] A dual *cis*-regulatory module has been proposed to explain their regulatory actions, in which the proximal and distal enhancer elements function redundantly, rather than cooperatively, to govern Atoh7 expression.[22] We reasoned that the collective disruption of both elements would severely impact Atoh7 expression and RGC genesis and tested this prediction by targeting a genomic region that contains both elements. We show that mice harboring such a deletion exhibit a dramatic effect on ocular structure and function. In fact, the phenotypic manifestations in *Atoh7-TEN*$^{-/-}$ mice broadly match what is observed in the Atoh7 gene KO.[7,8] Such a resemblance was also observed at the transcriptional level at the time of RGC genesis, whereby the developing retina suffered a severe downregulation of Atoh7 and its well-known downstream GRN.

Defects in retinal angiogenesis upon Atoh7 inactivation have been well documented.[12,21,32] Evidence suggests that deficiencies in adult blood vasculature are secondary to loss of RGCs and optic nerve.[22,32] Specifically, it was shown that RGCs provide instructive signals that facilitate vasculature-forming astrocyte colonization of the retina periphery and that disruption of the optic disc structure hinders the ability of astrocytes to migrate.[12,22,32] Additionally, Atoh7-TEN and Atoh7 gene KOs also suffer from persistent hyperplastic primary vitreous,[7,21] and our transcriptional data indicated a significant dysregulation of key regulators of angiogenesis in the *Atoh7-TEN*$^{-/-}$ retina, including Ndp (Norrin; 0.6-fold reduction; adjusted $p < 0.05$), Pdgfd (2-fold upregulation, adjusted $p < 0.05$), and shh (>0.99-fold reduction; adjusted $p < 0.05$; Table S2).[60–62]

In contrast, deletion of the Atoh7 remote enhancer led to more subtle defects in retinogenesis, despite a strong reduction in Atoh7 expression. Our data are consistent with previous results produced using an independent mouse line harboring a different mutant allele.[22] Specifically, the Atoh7-REN deletions generated by Miesfeld and co-workers are larger in size (~5,700 vs. 4,900 bp in this study). Still, both enhancer deletions considerably overlap and span the remote enhancer region as defined by chromatin marks at E14.5, hence the phenotypic similarity. Transcriptionally, we found that most of the RGC GRNs are expressed in the developing retina from *Atoh7-REN*$^{-/-}$, in agreement with immunostaining data from the study by Miesfeld and co-workers.[22] Our data may imply that the retinal precursor cells in *Atoh7-REN*$^{-/-}$ retina retained a sufficient residual Atoh7 dosage to sustain the transcription of the GRN factors underlying RGC differentiation. The residual expression of *Atoh7* in retinal precursor cells is likely conferred by the intact proximal regulato ry element near the *Atoh7* TSS,[22] a hypothesis that needs to be further tested.

The role of Atoh7 in regulating axon growth and guidance is not well studied because Atoh7 mutant mice effectively do not develop the optic nerve.[7,8] However, recent studies have begun to shed light on this aspect of Atoh7 function.[22,63] Our data revealed that Atoh7 is required for the expression of several axonogenesis genes, of which the collective dysregulation may be responsible for the observed defects in the dLGN retinotectal map. The robust upregulation of Robo3, an axon guidance cue that regulates axon turning, is particularly striking, given that Robo3 is not normally expressed in the retina. Interestingly, Robo3 repression appears to be selectively mediated by PRC2, a well-studied histone-modifying complex that is associated with gene repression.[47,64] While the exact molecular underpinnings of Robo3 repression remain unknown, a possible mechanism might involve Atoh7-mediated recruitment of PRC2 to the Robo3 promoter. Proneural bHLH factors are known to interact with positive regulators of chromatin accessibility such as the chromatin remodeling factor Brg1, supporting our reasoning.[65] However, we could not find evidence of Atoh7 occupancy on the Robo3 promoter in published Atoh7 CU-T&RUN data,[63] suggesting that Atoh7-mediated regulation of Robo3 may be indirect or that Atoh7 recruitment to the Robo3 genomic region in RGC precursors is transient. Still, our data suggest that proneural bHLH factors may utilize repressive chromatin-based mechanisms to control gene expression during retinogenesis, an exciting hypothesis that requires further work in the future.

Limitations of the study

Our work addressed the requirements of the entire regulatory landscape of Atoh7 and its remote enhancer to RGC genesis and axonogenesis. However, the role of the Atoh7 proximal enhancer in the context of the remote enhancer mutant condition was not established. Additionally, the molecular mechanisms by which Atoh7 affects axonogenesis and iRGC development remain unclear. Specifically, how Atoh7 loss of function leads to the upregulation of Robo3 and subsequent defects in axonal innervations is unknown.

STAR★METHODS

Detailed methods are provided in the online version of this paper and include the following:

RESOURCE AVAILABILITY

Lead contact—Further information and requests for resources and reagents should be directed to and will be fulfilled by the lead contact, Issam Aldiri (aldirii@pitt.edu).

Materials availability—All unique/stable reagents generated in this study are available from the lead contact with a completed materials transfer agreement.

Data and code availability

- This paper does not report original code.
- High-throughput sequencing data have been deposited in the Gene Expression Omnibus(GEO)database under accession number GSE245549.
- Any additional information required to reanalyze the data reported in this paper is available from the lead contact upon request.

EXPERIMENTAL MODEL AND STUDY PARTICIPANT DETAILS

Animals—Mice: All animals were housed and maintained in accordance with the guidelines set forth by the Institutional Animal Care and Use Committee of the University of Pittsburgh. C57 BL/6 mice were purchased from Jackson Laboratory. B6.FVB(Cg)-Tg(Slc6a4-cre) ET33Gsat/Mmucd (referred to as *Slc6a4*:*Cre*, RRID:MMRRC 031028-UCD to which they were donated by Dr. Nathaniel Heintz), B6.Cg-Gt(ROSA)26Sor$^{tm6(CAG–ZsGreen1)Hze}$/J mice (referred to as *R26R*^{ZsGreen}) was purchased from Jackson Laboratory (007906, RRID:IMSR_JAX:007906).

Zebrafish: Zebrafish (Danio rerio) were maintained in a controlled environment at a temperature of 28.5°C, following a 14-h light/10-h dark cycle. All procedures conducted in this research were granted approval by the Institutional Animal Care and Use Committee of The University of Texas at Austin and adhered to the guidelines outlined in the National Institutes of Health Guide for the Care and Use of Laboratory Animals. The transgenic lines used in this study are Tg(*vsx2*:Gal4-Vp16)^{mw39} and Tg(*14XUAS*:Kaedêrk7) referred as *vsx2*:Gal4 and *UAS*:kaede, respectively.

Mice enhancer knockouts—Generation of the enhancer knockout lines has been performed as previously described.[72] B6D2 (C57 BL/6J × DBA/2J F1) females (6–8 weeks old) were stimulated by intraperitoneal administration of 5 IU of PMSG (Pregnant Mare Serum Gonadotropin) at 3:30 p.m. on day 1, 5 IU of hCG (human chorionic gonadotropin) 48 h after PMSG injection, then mated to B6D2 F1 stud males. Following morning, embryos were collected from oviducts, and cultured in KSOM medium at 5% CO2, 37°C until electroporation. Embryos were further electroporated with 100 ng of Cas9 protein and 200 ng/μL of gRNAs each in Opti-MEM medium. gRNAs were chosen based on off-target analysis and tested prior to embryo injection for activity in mouse N2A cells using targeted next generation sequencing as previously described.[73] Electroporation was performed using the Super electroporator NEPA21 type II and CUY 501-1-1.5 electrode (NEPA GENE Co. Ltd, Chiba, Japan) at the conditions: poring pulse (voltage 40 V, pulse length 2.5 ms, pulse interval 50 ms, number of pulses 4, decay rate 10%, polarity +); transfer pulse (voltage 7V, pulse length 50 ms, pulse interval 50 ms, number of pulses 5, decay rate 40%, polarity +/=). After electroporation, the embryos were washed two times in KSOM medium, then cultured in KSOM medium overnight at 5% CO2,37°C. Subsequently, the two cell stage embryos were transferred to the oviducts of pseudo-pregnant CD1 females (0.5 dpc). The resulting founder animals (P0) were genotyped using PCR and Illumina Mi-Seq to identify mice with desired deletions. Adult animals positive for deletion were backcrossed to C57 BL/6J to generate WT, heterozygous and homozygous animals, in which Sanger sequencing was used to confirm genotyping. Deletion coordinates are depicted in the main figures.

Generation of zebrafish Tg (*vsx2*:Gal4;*5xUAS*:robo3b.1-p2A-tdTomatoCAXX)—The pMErobo3b.1 and p3E-p2A-tdTomatoCAXX plasmids were generously donated by Dr. Wolfgang Driever (The Albert–Ludwigs–Universität Freiburg).[66] LR Clonase II Plus was used for Multisite Gateway assembly reactions,[74] using p5E-UAS (20 ng), pMErobo3b.1 (without stop codon) (45 ng), p3E-p2A-tdTomatoCAXX (28 ng), and pDestTol2CG2 (102 ng) plasmids. Tol2 mRNA was synthesized from pCS2FA-transposase using the Ambion mMessage mMachine Sp6 *in vitro* transcription kit (Thermo Fisher Scientific, AM1340). Tol2 mRNA (75pg) was co-injected with pDestTol2CG2;*5x*UAS:robo3b.1-P2A-tdTomatoCAAX (30 pg) into *vsx2*:Gal4 embryos at the 1-cell stage. Embryos were raised to adulthood and subsequently outcrossed for founder screening.

METHOD DETAILS

Confocal laser scanning Microscopy and image processing of zebrafish—F_1 embryos derived from *vsx2*:Gal4;*5x*UAS:robo3b.1-p2A-tdTomatoCAXX and control *vsx2*:Gal4;*14xUAS*:Kaede were treated with 1-phenyl-2-thiourea (PTU; Sigma-Aldrich) from 6hpf to 5dpf to inhibit pigmentation. The fluorescence of GFP and tdTomato was initially assessed using a fluorescent dissecting microscope. For a more in-depth analysis of fluorescence, live 5-day post-fertilization (dpf) larvae were immobilized in 1% low-melting agarose and anesthetized with MS-222 (Tricaine, Sigma-Aldrich, St. Louis, MO, USA) prior to imaging. Confocal images were acquired using a Nikon AXR upright microscope equipped with a 40x water immersion objective. Image stacks were recorded with a z-spacing of 2 μm. Subsequent processing of the images for presentation was conducted using

ImageJ (Fiji) software. The final image was prepared using Adobe Photoshop CC 2024 (Adobe Systems Inc., San Jose, CA, USA).

Retinal histology

H&E staining: To examine the overall morphology of the adult retina, the whole eyes from WT and KO mice were fixed in 4% paraformaldehyde. Fixed eyes were dehydrated in a series of graded ethanol (70%, 80%, 95% 100%) for 20 min each. After three changes in xylene for 20 min each, the eyes were embedded in molten paraffin wax in an automated tissue processor (Sakura Tissue-Tek VIP 5). FFPE blocks were sectioned at 5 μm thickness using Leica 2235 rotary microtome, stained with H&E (Hematoxylin and Eosin) and imaged with bright field microscope (Olympus). All histological procedures were performed following the protocols established by our histology core facility's guidelines.

Immunostaining

The immunostaining on embryonic eyes (E14.5) and postnatal retinae (P21) was performed as previously described.[72] Briefly, wild-type and mutant eyes were enucleated and fixed in 4% formaldehyde overnight in 4°C, followed by a PBS wash for 5 min. The tissues were subsequently subjected to graded concentrations of sucrose (5%, 10%, 20% and 40%) in 1X PBS (pH = 7.4) until they sank and then cryoembedded in a mixture of 40% sucrose and OCT (Optimum Cutting Temperature) in 1:1 (v/v) ratio, and later cryosectioned at 14–16 μm thickness. Retinae were washed three times with PBST (0.5% Triton X-), blocked with 1% BSA in 1X PBS for 1hr and then incubated in primary antibody overnight at 4°C. The sections were washed 3 × 5 min with 1X PBS and then incubated in fluorescent dye-conjugated secondary antibody for 1 h at room temperature. After labeling, sections were incubated in 2 μg/mL Hoechst 33342 stain (Invitrogen H3570) for 10 min, washed with 1XPBS, then mounted with ProLong Glass Antifade Mountant (Invitrogen P36980). Images were acquired on Olympus Fluoview Confocal microscope (v 4.2). Antibodies used in the present study are listed in key resource table.

Axonal projection assay—P30 animals were anesthetized with ketamine/xylazine. 2 μL of2 μg/μL of Alexa Fluor 488 and 555 conjugated cholera toxin β subunit (CTB) (ThermoFisher, C34775, C22843) were injected into the left and right retina of the same animal respectively 2 days before euthanasia. Animals were then humanely euthanized with CO2 and perfused with 4% paraformaldehyde (PFA) following PBS. The heads were cut and post-fixed in 4% PFA overnight at 4°C and washed with PBS for further analysis. For cryosectioning, the whole brain was incubated in 20% sucrose in PBS for 24h and then 30% sucrose in PBS for 48 h at 4°C, and embedded with Tissue-Tek O.C.T. (Optimum cutting temperature). 30 μm dLGN cryosections were prepared and mounted with Fluoro-Gel mounting medium (Electron Microscopy Sciences, 17985-11). Two dLGN cryosections per animal were used to quantify the mean intensity of CTB-555 fluorescence (ipsilateral axons), and the average of the intensity values from two sections per animal/condition was provided, and normalized to the control samples.

Analysis of ipsilateral and contralateral RGCs—For quantification of E14.5 and E17.5 ipsilateral and contralateral RGCs, 14 μm coronal retinal cryosections were prepared,

and the number of $Zic2^+$ and/or $Islet1/2^+$ cells within 150 μm from the peripheral edge of VT and DT retina was counted in both eyes of 4 sections (E17.5) and 2 sections (E14.5) at the level of the optic nerve per embryo. For quantification of E17.5 ZsGreen-$SERT^+$ ipsilateral RGCs on 14 μm coronal retinal cryosections, ZsGreen-$SERT^+$ cells within 150 μm from the peripheral edge of VT retina was counted in both eyes of 4 sections. These experiments were repeated in three embryos each condition.

Electroretinography (ERG)—ERG was performed as previously described.[72] Prior to ERG testing, mice were subjected to dark adaptation overnight. Following day, mice were anesthetized intraperitoneally with ketamine/xylazine (80 mg/kg bw/7 mg/kg bw) and allowed to become completely sedated. Both the eyes were treated with 1% Tropicamide and 2.5% phenylephrine hydrochloride solution for the dilation of pupil. The mouse was positioned on a heating platform and reference electrodes were gently applied on the central cornea. The scotopic ERG recordings were obtained at light intensities ranging from 0.0001 cd s/m^2 to 100 cd s/m^2. ERG responses of dark-adapted eyes to seven flashes from were recorded and averaged from ten sweeps per flash intensity with inter-sweep intervals of 10–30 s. After exposure to 10 cd/m^2 illumination for 10 min, the photopic ERG responses were recorded from the light-adapted eyes in response to flashes from 0.01 cd s/m^2 to 100 cd s/m^2 in addition to a 10 cd/m^2 background light. ERGs were analyzed for six mice per group by plotting the amplitude (μV) of a-and b-waves against varied light intensities (cd.s/m^2) over the entire stimulus range. The a-wave amplitude was measured from the pre-stimulus baseline to the peak negative voltage, and the b-wave amplitude was measured from the a-wave trough to the b-wave peak.

RNA sequencing—Fresh retinae were placed in TRIReagent (Zymo Research R2050-1-50), and RNA was extracted according to Direct-zol RNA MiniPrep kit protocol (Zymo Research R2050). RNA integrity was determined using 4200 Agilent Tapestation (Agilent Technologies, Santa Clara, CA). Stranded total RNA libraries were prepared following manufacturer's instructions Illumina TruSeq Stranded RNA (Ribo-Zero) with the following modifications: Total RNA input is depleted for rRNA and fragmented. Random primers initiate first and second strand cDNA synthesis. Adenylation of 3′ ends is followed by adapter ligation and library amplification with indexing. The sequencing was run on high output 150 cycles flowcell with read length 2×75 using the Sequencing Platform NextSeq500.

Analysis of bulk RNA-Seq—Raw sequencing reads first went through the pipeline of quality control [QC] using Trimmomatic. After pre-processing, surviving reads were aligned to mouse reference genome mm10 by STAR aligner and quantified by read count using HTSeq tool. Differential expression analysis comparing wild-type and knock-out samples were performed by R package DESeq2. Significant changes in gene expression were defined by adjusted *p*-value lower than 0.05 (FDR = 5%) and fold change greater than 1.5. All the bioinformatics and biostatistical analysis were performed by default parameters.

Optical coherence tomography (OCT) imaging—Animals were anesthetized by intraperitoneal injection of ketamine (80 mg/kg) and xylazine (8 mg/kg) and their pupils

were dilated with 1% tropicamide followed by 2.5% phenylephrine. To keep the cornea moist, sterile irrigating salt solution (Alcon Laboratories Inc.) was applied frequently throughout the experiments. Body temperature was maintained at 38°C with a heating pad. One eye of each animal was randomly chosen for the *in vivo* OCT retinal imaging. OCT scans were acquired at a visible light OCT (vis-OCT) prototype developed at PITT OCT Lab which operates at 560 nm with an A-line sampling rate of 50 kHz.[31] The vis-OCT provides a 1.2-μm axial resolution in tissue and ~6-μm lateral resolution. The incident power on the cornea was 0.8 mW. At each image session, volumetric raster scans consisting of 500 × 2×500 A-lines covering a 1.5 × 1.5-mm field of view were acquired for retinal structure and angiography analysis. Customized software written in LABVIEW with real-time OCT visualization was used to record the interferogram by a line scan camera. Scan processing were performed in MATLAB. OCT angiography (OCTA) was calculated with spilt-spectrum amplitude-decorrelation angiography (SSADA) algorithm. Retinal layers were first automatically segmented using a graph-searching method and then manually corrected to ensure boundary accuracy. To evaluate retinal damages in the Atoh7 mice, we performed retinal layer thickness measurements on two slabs: the total retina and ganglion cell complex (GCC). The whole retina *en face* images were projected from OCT total retinal slab. RGC axon bundle *en face* images were projected from OCT nerve fiber layer (NFL). Retinal vasculature *en face* images were projected from OCTA total retinal slab.

Sc-ATAC-seq—C57BL/6J E14.5 retinae were collected and dissociated using Postnatal dissociation kit (MACS #130-094-802), according to the manufacturer protocol. Retinal cell suspension was filtered through 70-μm strainer (MACS #130-098-462) and then PBS+0.1 %BSA was added to bring the total volume to 10 mL. After centrifuging to clear debris, supernatant was discarded and cells were resuspended in 250uL of PBS+ 0.1 %BSA. After determining cell numbers by hemocytometer, retinal cells were further diluted to a concentration of 1 million cells per mL. Cell suspension was spun down at 300 g for 5 min at 4°C. Supernatant was discarded and cells were resuspended in 100 μL of Cold Lysis Buffer (10mM Tris 7.4, 10mM NaCl, 3mM MgCl2, 0.1% Tween 20, 0.1%NP40, 0.01% Digitonin, 1% BSA) and incubated on ice for 3 min. One mL of chilled Wash Buffer (10mM Tris 7.4, 10mM NaCl, 3mM MgCl2, 0.1% Tween 20, 1% BSA) was added and the cell suspension was spun again at 500 g for min at 4C. Nuclei were resuspended in Diluted Nuclei Buffer (10X genomics single cell ATAC kit) and cell concentration was determined by hemocytometer. Approximately 5000 nuclei were used in transposition reaction and further processed according to the 10X genomics single cell ATAC protocol (Chromium Single Cell ATAC Reagent Kits protocol CG000168). scATAC-seq libraries were normalized and pooled as per manufacturer protocol (Illumina). Sequencing of two technical replicas was performed using NovaSeq 6000 platform (Illumina) with 50bp/49bp paired-end reads on an SP-100 cycles flow cell for a total of 800M reads. Samples were sequenced a the UPMC Genome Center.

Analysis of scATAC-seq data—Processed data were analyzed using the Signac (https://CRAN.Rproject.org/package=Signac) and Seurat (https://CRAN.Rproject.org/package=Seurat) R software packages, and the EnsDb.Mmusculus.v79 annotation package was used for moue genome annotation. We used the following criteria to filter cells for

each sample separately: Peak region fragments between 10,000 and 500,000, Reads in peaks >15%, Blacklist ratio <0.05.

Nucleosome signal <4, TSS enrichment >2.

Samples were then aligned by intersecting peak calls from both samples and keeping only peaks where the overlap in at least one sample reaches 50%; peaks larger than 10kb and peaks smaller than 50bp were discarded, then fragments were re-counted for the aligned peak set. Peaks/features detected in less than 10 cells were discarded, as were cells with fragments detected in less than 200 features. This yielded 1,823 cells (837 cells from sample A1 and 986 cells from sample A2) with fragments in 113,567 peaks/features for further analysis. For these cells we recovered 70,772 fragments in (aligned) peaks per cell on average (IQR: 51,734–87,589), and the average number of detected peaks/features in a cell was 39,295.97 (IQR: 26,856–35,281). Term frequency inverse document frequency normalization was applied followed by principal component analysis, and principal components 2 to 10 were used for UMAP dimension reduction (parameters: metric = “cosine”, n.neighbors = 30L, min.dist = .2, spread = .2) and clustering.

Gene accessibility/activity was calculated by counting fragments in peaks/features overlapping a gene’s transcripts and promoters and subsequent normalization.

(NormalizeDatafunction from the Seurat package using the “LogNormalize” method).

Marker genes for clusters (based on accessibility/activity) were obtained using the FindAllMarkers function (parameters: test.use = “roc” and logFC.threshold = log(1.5)) provided by the Seurat R package, which was also used for generating gene activity heatmaps, violin plots and coverage plots. Differentially accessible peaks were calculated in two ways. First, for each cluster using the FindAllMarkers function provided by the Seurat package (parameters: test.use = “roc”, logFC.threshold = log(1.5), pseudocount.use = .1). Second, we combined clusters 0–3 and clusters 4–8 and used FindAllMarkers again (same parameters as before).

Co-embedding scRNA-seq and scATAC-seq datasets—Firstly, gene activity scores were derived from scATAC-seq data utilizing the GeneActivity function available in the Signac package. Subsequently, cell types within the scRNA-seq dataset were annotated through label transfer, employing imputed gene activity scores from scATAC-seq as the reference. Following this, we embarked on co-embedding scATAC-seq with scRNA-seq data. We identified the anchors between scRNA-seq and scATAC-seq datasets by inputting gene expression profiles from scRNA-seq and gene activity scores derived from scATAC-seq into the canonical correlation analysis. Subsequent to anchor identification, we merged the datasets by leveraging these computed anchor points, achieving a unified representation of the scRNA-seq and scA-TAC-seq data.

GO analysis—DAVID was used to analyze significantly changed genes in *Atoh7* enhancer knockouts with default settings.[75,76]

Single cell-RNA-Seq—Retinae from E14.5 embryos were freshly dissected, and cells were dissociated using Macs Miltenyi Adult Brain Tissue Dissociation Kit (130-107-677), according to manufacturer's recommendations. The cells were resuspended in 0.1% BSA in D-PBS and processed immediately for scRNA-seq. Samples were prepared for single cell analysis using a 10x Chromium Single Cell 3′ v3.1 kit. The resulting libraries were pooled, and an additional targeted gene enrichment protocol was performed using 10x Chromium Targeted Gene Expression kit. Samples were submitted for deep sequencing on Illumina Novaseq S2 or SP flow cells at the UPMC Genome Center.

The sequenced scRNA-seq libraries were processed and aligned to the mm10 mouse reference genome using Cell Ranger software (version 6.1.2) by 10x Genomics. Unique molecular identifier (UMI) counts were then aggregated for each barcode. To distinguish cells from background noise, cell calling was conducted on the full raw UMI count matrices, yielding filtered UMI count matrices, which recovered 12,627 and 14,458 cells from WT mice's retinae, as well as 13,864 and 15,716 cells from ATOH7-REN−/− mice's retinae.

Upon import into R, the filtered UMI count matrices were subjected to analysis using the R package Seurat (version 4.0.1). Cells from both WT and ATOH7-REN−/− mice were pooled, revealing negligible disparities among the four samples regarding gene count, total UMI count, and the proportion of mitochondrial genes. Subsequently, pooled cells underwent filtering, adhering to the following criteria: a minimum detection threshold of 200 genes, a maximum detection threshold of 10,000 genes, and a cap of 25% for mitochondrial genes. Normalization of the UMI count data for the remaining cells was carried out using regularized negative binomial regression (SCTransform), with the mitigation of potential confounding effects from mitochondrial mapping percentage. To enhance normalization speed, glmGamPoi was integrated into the process. The identification of 3,000 highly variable genes was instrumental in performing principal component analysis (PCA) for dimensionality reduction. To counteract batch effects, Harmony was applied to the first 50 components of PCA reduction, with distinct samples serving as covariates and the maximum number of rounds set as 20. UMAP dimensionality reduction was employed with the first 50 Harmony-adjusted components as input to visualize cells. Subsequently, cells were clustered using the Shared Nearest-neighbor (SNN) graph, leveraging the original Louvain algorithm with a resolution of 0.2.

In the preliminary clustering, clusters comprising low-quality cells, as indicated by the prevalence of dominant mitochondrial, ribosomal, crystallin, and hemoglobin genes, were identified. These clusters were subsequently excluded, and the normalization, batch correction, dimensionality reduction, and clustering processes were reiterated. The final clusters were delineated using the original Louvain algorithm with a resolution of 0.2. Markers for each cluster were identified through the FindAllMarkers function, utilizing a Wilcoxon Rank-Sum test with parameters only.pos = TRUE, min.pct = 0.25, and logfc.threshold = 0.25. The clusters were subsequently annotated based on the marker genes characteristic of each cluster.

FISH analysis—We conducted RNA *in-situ* hybridization analysis on 14 μm thick frozen sections of E14.5 retina using a two-stage Hybridization Chain Reaction (HCR) protocol

following the manufacturer's instructions (Molecular Instruments, Inc., Los Angeles, CA). Initially, slides were pre-warmed at 37°C for 10 min and then dehydrated in a series of graded alcohol (50%, 70%, and two changes of 100% ethanol) for 5 min each at room temperature. After a brief wash in 1X PBS, the sections were treated with a 10 μg/mL proteinase K solution (200 μL) for 10 min at 37°C. Following two 5-min washes in 1X PBS, the slides were placed in a pre-warmed humidified chamber at 37°C for 10 min with 200 μL of probe hybridization buffer. The sections were subsequently immersed overnight in a 37°C humidified chamber with 200 μL of the probe solution (prepared by mixing 6 μL of 1 μM stock with 200 μL of probe hybridization buffer). We utilized two HCR probe sets, Mouse-Robo3-B4 and Pou4f2-B1 (Molecular Instruments Inc.). Excess probes were removed by incubating the sections at 37°C in varying concentrations of probe wash buffer combined with 5× SSCT for 15 min each. Amplification was carried out using 6 pmol of hairpin h1 and 6 pmol of hairpin h2, prepared by snap cooling 5 μL of 3 μM stock in 200 μL of amplification buffer. Two HCR amplifiers (B4–546 and B1–488) were used specific to each probe set. Slides were coverslipped and incubated overnight (>12 h) in a dark, humidified chamber at room temperature. The following day, excess hairpins were removed through three washes in 5× SSCT for specified durations. Finally, the slides were mounted with anti-fade media and examined using a 40X objective on a laser-scanning confocal microscope (Olympus FluoView FV1000 confocal microscope; Olympus, Center Valley, PA).

Chromatin immunoprecipitation—ChIP experiments for mouse retina and cerebellum have been performed as previously described.[23] In brief, tissue was isolated and fixed in 1% FA for 10 min. TruChIP chromatin shearing kit (Covaris #520127) was used to prepare cells for shearing according to the manufacturer's protocol. iDeal ChIP-seq kit (Diagenode #C01010051) was used to perform ChIP on sheared chromatin using the following antibodies H3K27Ac (Abcam, Cat. # AB4729), H3K4me2 (Abcam, Cat. # AB7766), H3K27me3 (Millipore, Cat. # 07-449). Sequencing libraries were prepared using NEBNext Ultra II DNA Library Prep kit (NEB, Cat. #E7645) following the manufacturer's protocol. Sequencing was done at the Health Sciences Sequencing core of the Children's Hospital of Pittsburgh using Illumina NextSeq 2000. Sequencing reads were aligned to mouse (mm10) reference genome by Burrows-Wheeler Aligner (BWA) algorithm. Low-quality alignment and duplicate reads were removed by SAMtools. Standard MACS2 algorithm was used to call peaks, comparing matched treated and input samples. ChIP tracks were visualized with Integrative Genomics Viewer (IGV) and heat maps were generated using Pluto Bioinformatics platform.

QUANTIFICATION AND STATISTICAL ANALYSIS

Detailed explanations of statistical analyses and sample sizes (n) for each figure panel are provided in the legends. Mean values for each dataset are reported with their corresponding standard error of the mean (SEM) or standard deviation (SD) where appropriate. The comparisons for ERG waves under varying light intensities were conducted using two-way ANOVA in GraphPad Prism 9 software (San Diego, California USA. All other comparisons were analyzed using two-tailed student's T test. All p-values reported were deemed significant at a threshold of $p < 0.05$.

Supplementary Material

Refer to Web version on PubMed Central for supplementary material.

ACKNOWLEDGMENTS

We would like to acknowledge the Health Sciences Genomics Research Cores at the University of Pittsburgh and the Magee-Womens Research Institute's Genome Editing, Transgenic, and Virus (GETV) Core Facility. We thank the Genome Engineering and iPSC Center (GEiC) at the Washington University in St. Louis for gRNA validation and genotyping services. This work was supported by the Research to Prevent Blindness (RPB) career development award, NIH R01 (EY030861-01A1); a University of Pittsburgh start up fund for I.A.; and NIH R01 (EY029031) for J.M.G. This work was also supported by the University of Pittsburgh Center for Research Computing through the resources provided, NIH Core Grant P30 EY08098 to the Department of Ophthalmology, the Eye and Ear Foundation of Pittsburgh, and an unrestricted grant from RBP, New York, NY.

REFERENCES

1. Cepko CL, Austin CP, Yang X, Alexiades M, and Ezzeddine D (1996). Cell fate determination in the vertebrate retina. Proc. Natl. Acad. Sci. USA 93, 589–595. [PubMed: 8570600]
2. Livesey FJ, and Cepko CL (2001). Vertebrate neural cell-fate determination: lessons from the retina. Nat. Rev. Neurosci. 2, 109–118. 10.1038/35053522. [PubMed: 11252990]
3. Bassett EA, and Wallace VA (2012). Cell fate determination in the vertebrate retina. Trends Neurosci. 35, 565–573. 10.1016/j.tins.2012.05.004. [PubMed: 22704732]
4. Brzezinski JA 4th, Prasov L, and Glaser T (2012). Math5 defines the ganglion cell competence state in a subpopulation of retinal progenitor cells exiting the cell cycle. Dev. Biol. 365, 395–413. 10.1016/j.ydbio.2012.03.006. [PubMed: 22445509]
5. Brown NL, Kanekar S, Vetter ML, Tucker PK, Gemza DL, and Glaser T (1998). Math5 encodes a murine basic helix-loop-helix transcription factor expressed during early stages of retinal neurogenesis. Development 125, 4821–4833. [PubMed: 9806930]
6. Pan L, Deng M, Xie X, and Gan L (2008). ISL1 and BRN3B co-regulate the differentiation of murine retinal ganglion cells. Development 135, 1981–1990. 10.1242/dev.010751. [PubMed: 18434421]
7. Brown NL, Patel S, Brzezinski J, and Glaser T (2001). Math5 is required for retinal ganglion cell and optic nerve formation. Development 128, 2497–2508. [PubMed: 11493566]
8. Wang SW, Kim BS, Ding K, Wang H, Sun D, Johnson RL, Klein WH, and Gan L (2001). Requirement for math5 in the development of retinal ganglion cells. Genes Dev. 15, 24–29. [PubMed: 11156601]
9. Kondo H, Matsushita I, Tahira T, Uchio E, and Kusaka S (2018). Mutations in ATOH7 gene in patients with nonsyndromic congenital retinal nonattachment and familial exudative vitreoretinopathy (vol 37, pg 462, 2016). Ophthalmic Genet. 39, 553. 10.1080/13816810.2018.1477565. [PubMed: 29851533]
10. Keser V, Khan A, Siddiqui S, Lopez I, Ren H, Qamar R, Nadaf J, Majewski J, Chen R, and Koenekoop RK (2017). The Genetic Causes of Nonsyndromic Congenital Retinal Detachment: A Genetic and Phenotypic Study of Pakistani Families. Invest. Ophthalmol. Vis. Sci. 58, 1028–1036. 10.1167/iovs.16-20281. [PubMed: 28192794]
11. Kay JN, Finger-Baier KC, Roeser T, Staub W, and Baier H (2001). Retinal ganglion cell genesis requires lakritz, a zebrafish atonal homolog. Neuron 30, 725–736. 10.1016/S0896-6273(01)00312-9. [PubMed: 11430806]
12. Edwards MM, McLeod DS, Li R, Grebe R, Bhutto I, Mu X, and Lutty GA (2012). The deletion of Math5 disrupts retinal blood vessel and glial development in mice. Exp. Eye Res. 96, 147–156. 10.1016/j.exer.2011.12.005. [PubMed: 22200487]
13. Brzezinski JA 4th, Brown NL, Tanikawa A, Bush RA, Sieving PA, Vitaterna MH, Takahashi JS, and Glaser T (2005). Loss of circadian photoentrainment and abnormal retinal electrophysiology in Math5 mutant mice. Invest. Ophthalmol. Vis. Sci. 46, 2540–2551. 10.1167/iovs.04-1123. [PubMed: 15980246]

14. Gan L, Xiang M, Zhou L, Wagner DS, Klein WH, and Nathans J (1996). POU domain factor Brn-3b is required for the development of a large set of retinal ganglion cells. P Natl Acad Sci USA 93, 3920–3925. 10.1073/pnas.93.9.3920.
15. Wu F, Kaczynski TJ, Sethuramanujam S, Li R, Jain V, Slaughter M, and Mu X (2015). Two transcription factors, Pou4f2 and Isl1, are sufficient to specify the retinal ganglion cell fate. P Natl Acad Sci USA 112, E1559–E1568. 10.1073/pnas.1421535112.
16. Kim S, and Wysocka J (2023). Deciphering the multi-scale, quantitative cis-regulatory code. Mol. Cell 83, 373–392. 10.1016/j.molcel.2022.12.032. [PubMed: 36693380]
17. Yuan X, Song M, Devine P, Bruneau BG, Scott IC, and Wilson MD (2018). Heart enhancers with deeply conserved regulatory activity are established early in zebrafish development. Nat. Commun. 9, 4977. 10.1038/s41467-018-07451-z. [PubMed: 30478328]
18. Riesenberg AN, Le TT, Willardsen MI, Blackburn DC, Vetter ML, and Brown NL (2009). Pax6 Regulation of Math5 During Mouse Retinal Neurogenesis. Genesis 47, 175–187. 10.1002/dvg.20479. [PubMed: 19208436]
19. Hutcheson DA, Hanson MI, Moore KB, Le TT, Brown NL, and Vetter ML (2005). bHLH-dependent and -independent modes of Ath5 gene regulation during retinal development. Development 132, 829–839. 10.1242/dev.01653. [PubMed: 15677728]
20. Ghiasvand NM, Rudolph DD, Mashayekhi M, Brzezinski JA, Goldman D, and Glaser T (2011). Deletion of a remote enhancer near ATOH7 disrupts retinal neurogenesis, causing NCRNA disease. Nat. Neurosci. 14, 578–586. 10.1038/nn.2798. [PubMed: 21441919]
21. Prasov L, Masud T, Khaliq S, Mehdi SQ, Abid A, Oliver ER, Silva ED, Lewanda A, Brodsky MC, Borchert M, et al. (2012). ATOH7 mutations cause autosomal recessive persistent hyperplasia of the primary vitreous. Hum. Mol. Genet. 21, 3681–3694. 10.1093/hmg/dds197. [PubMed: 22645276]
22. Miesfeld JB, Ghiasvand NM, Marsh-Armstrong B, Marsh-Armstrong N, Miller EB, Zhang P, Manna SK, Zawadzki RJ, Brown NL, and Glaser T (2020). The Atoh7 remote enhancer provides transcriptional robustness during retinal ganglion cell development. Proc. Natl. Acad. Sci. USA 117, 21690–21700. 10.1073/pnas.2006888117. [PubMed: 32817515]
23. Aldiri I, Xu B, Wang L, Chen X, Hiler D, Griffiths L, Valentine M, Shirinifard A, Thiagarajan S, Sablauer A, et al. (2017). The Dynamic Epigenetic Landscape of the Retina During Development, Reprogramming, and Tumorigenesis. Neuron 94, 550–568.e10. 10.1016/j.neuron.2017.04.022. [PubMed: 28472656]
24. Lyu P, Hoang T, Santiago CP, Thomas ED, Timms AE, Appel H, Gimmen M, Le N, Jiang L, Kim DW, et al. (2021). Gene regulatory networks controlling temporal patterning, neurogenesis, and cell-fate specification in mammalian retina. Cell Rep. 37, 109994. 10.1016/j.celrep.2021.109994. [PubMed: 34788628]
25. Finkbeiner C, Ortuño-Lizarán I, Sridhar A, Hooper M, Petter S, and Reh TA (2022). Single-cell ATAC-seq of fetal human retina and stem-cell-derived retinal organoids shows changing chromatin landscapes during cell fate acquisition. Cell Rep. 38, 1–16. 10.1016/j.celrep.2021.110294.
26. Zhang XM, Hashimoto T, Tang R, and Yang XJ (2018). Elevated expression of human bHLH factor ATOH7 accelerates cell cycle progression of progenitors and enhances production of avian retinal ganglion cells. Sci. Rep. 8, 6823. 10.1038/s41598-018-25188-z. [PubMed: 29717171]
27. Cherry TJ, Yang MG, Harmin DA, Tao P, Timms AE, Bauwens M, Allikmets R, Jones EM, Chen R, De Baere E, and Greenberg ME (2020). Mapping the cis-regulatory architecture of the human retina reveals noncoding genetic variation in disease. Proc. Natl. Acad. Sci. USA 117, 9001–9012. 10.1073/pnas.1922501117. [PubMed: 32265282]
28. Stuart T, Butler A, Hoffman P, Hafemeister C, Papalexi E, Mauck WM 3rd, Hao Y, Stoeckius M, Smibert P, and Satija R (2019). Comprehensive Integration of Single-Cell Data. Cell 177, 1888–1902.e21. 10.1016/j.cell.2019.05.031. [PubMed: 31178118]
29. Ranzoni AM, Tangherloni A, Berest I, Riva SG, Myers B, Strzelecka PM, Xu J, Panada E, Mohorianu I, Zaugg JB, and Cvejic A (2021). Integrative Single-Cell RNA-Seq and ATAC-Seq Analysis of Human Developmental Hematopoiesis. Cell Stem Cell 28, 472–487.e7. 10.1016/j.stem.2020.11.015. [PubMed: 33352111]

30. Miesfeld JB, Glaser T, and Brown NL (2018). The dynamics of native Atoh7 protein expression during mouse retinal histogenesis, revealed with a new antibody. Gene Expr. Patterns 27, 114–121. 10.1016/j.gep.2017.11.006. [PubMed: 29225067]

31. Pi S, Camino A, Zhang M, Cepurna W, Liu G, Huang D, Morrison J, and Jia Y (2017). Angiographic and structural imaging using high axial resolution fiber-based visible-light OCT. Biomed. Opt Express 8, 4595–4608. 10.1364/BOE.8.004595. [PubMed: 29082087]

32. O'Sullivan ML, Puñal VM, Kerstein PC, Brzezinski JA 4th, Glaser T, Wright KM, and Kay JN (2017). Astrocytes follow ganglion cell axons to establish an angiogenic template during retinal development. Glia 65, 1697–1716. 10.1002/glia.23189. [PubMed: 28722174]

33. Stahl A, Connor KM, Sapieha P, Chen J, Dennison RJ, Krah NM, Seaward MR, Willett KL, Aderman CM, Guerin KI, et al. (2010). The mouse retina as an angiogenesis model. Invest. Ophthalmol. Vis. Sci. 51, 2813–2826. 10.1167/iovs.10-5176. [PubMed: 20484600]

34. Shastry BS (2009). Persistent hyperplastic primary vitreous: congenital malformation of the eye. Clin. Exp. Ophthalmol. 37, 884–890. 10.1111/j.1442-9071.2009.02150.x. [PubMed: 20092598]

35. Morita A, Mori A, Arima S, Sakamoto K, Nagamitsu T, Ishii K, and Nakahara T (2018). Transient phenotypic changes in endothelial cells and pericytes in neonatal mouse retina following short-term blockade of vascular endothelial growth factor receptors. Dev. Dynam. 247, 699–711. 10.1002/dvdy.24614.

36. Feng L, Xie ZH, Ding Q, Xie X, Libby RT, and Gan L (2010). MATH5 controls the acquisition of multiple retinal cell fates. Mol. Brain 3, 36. 10.1186/1756-6606-3-36. [PubMed: 21087508]

37. Wu F, Bard JE, Kann J, Yergeau D, Sapkota D, Ge Y, Hu Z, Wang J, Liu T, and Mu X (2021). Single cell transcriptomics reveals lineage trajectory of retinal ganglion cells in wild-type and Atoh7-null retinas. Nat. Commun. 12, 1465. 10.1038/s41467-021-21704-4. [PubMed: 33674582]

38. Dennis G Jr., Sherman BT, Hosack DA, Yang J, Gao W, Lane HC, and Lempicki RA (2003). DAVID: Database for Annotation, Visualization, and Integrated Discovery. Genome Biol. 4, P3. [PubMed: 12734009]

39. Clark BS, Stein-O'Brien GL, Shiau F, Cannon GH, Davis-Marcisak E, Sherman T, Santiago CP, Hoang TV, Rajaii F, James-Esposito RE, et al. (2019). Single-Cell RNA-Seq Analysis of Retinal Development Identifies NFI Factors as Regulating Mitotic Exit and Late-Born Cell Specification. Neuron 102, 1111–1126. 10.1016/j.neuron.2019.04.010. [PubMed: 31128945]

40. Bickford ME, Zhou N, Krahe TE, Govindaiah G, and Guido W (2015). Retinal and Tectal "Driver-Like" Inputs Converge in the Shell of the Mouse Dorsal Lateral Geniculate Nucleus. J. Neurosci. 35, 10523–10534. 10.1523/JNEUROSCI.3375-14.2015. [PubMed: 26203147]

41. Kerschensteiner D, and Guido W (2017). Organization of the dorsal lateral geniculate nucleus in the mouse. Vis. Neurosci. 34, E008. 10.1017/S0952523817000062. [PubMed: 28965501]

42. Sitko AA, Kuwajima T, and Mason CA (2018). Eye-specific segregation and differential fasciculation of developing retinal ganglion cell axons in the mouse visual pathway. J. Comp. Neurol. 526, 1077–1096. 10.1002/cne.24392. [PubMed: 29322522]

43. Rebsam A, Petros TJ, and Mason CA (2009). Switching retinogeniculate axon laterality leads to normal targeting but abnormal eye-specific segregation that is activity dependent. J. Neurosci. 29, 14855–14863. 10.1523/JNEUROSCI.3462-09.2009. [PubMed: 19940181]

44. Nakamoto C, Durward E, Horie M, and Nakamoto M (2019). Nell2 regulates the contralateral-versus-ipsilateral visual projection as a domain-specific positional cue. Development 146, dev170704. 10.1242/dev.170704. [PubMed: 30745429]

45. Pak JS, DeLoughery ZJ, Wang J, Acharya N, Park Y, Jaworski A, and Özkan E (2020). NELL2-Robo3 complex structure reveals mechanisms of receptor activation for axon guidance. Nat. Commun. 11, 1489. 10.1038/s41467-020-15211-1. [PubMed: 32198364]

46. Clark BS, Winter M, Cohen AR, and Link BA (2011). Generation of Rab-based transgenic lines for in vivo studies of endosome biology in zebrafish. Dev. Dynam. 240, 2452–2465. 10.1002/dvdy.22758.

47. Aldiri I, and Vetter ML (2012). PRC2 during vertebrate organogenesis: a complex in transition. Dev. Biol. 367, 91–99. 10.1016/j.ydbio.2012.04.030. [PubMed: 22565092]

48. Ku M, Koche RP, Rheinbay E, Mendenhall EM, Endoh M, Mikkelsen TS, Presser A, Nusbaum C, Xie X, Chi AS, et al. (2008). Genomewide analysis of PRC1 and PRC2 occupancy identifies two

classes of bivalent domains. PLoS Genet. 4, e1000242. 10.1371/journal.pgen.1000242. [PubMed: 18974828]

49. Zhang J, Taylor RJ, La Torre A, Wilken MS, Cox KE, Reh TA, and Vetter ML (2015). Ezh2 maintains retinal progenitor proliferation, transcriptional integrity, and the timing of late differentiation. Dev. Biol. 403, 128–138. 10.1016/j.ydbio.2015.05.010. [PubMed: 25989023]
50. Finogenova K, Bonnet J, Poepsel S, Schäfer IB, Finkl K, Schmid K, Litz C, Strauss M, Benda C, and Müller J (2020). Structural basis for PRC2 decoding of active histone methylation marks H3K36me2/3. Elife 9, e61964. 10.7554/eLife.61964. [PubMed: 33211010]
51. Kuwajima T, Soares CA, Sitko AA, Lefebvre V, and Mason C (2017). SoxC Transcription Factors Promote Contralateral Retinal Ganglion Cell Differentiation and Axon Guidance in the Mouse Visual System. Neuron 93, 1110–1125.e5. 10.1016/j.neuron.2017.01.029. [PubMed: 28215559]
52. Herrera E, Brown L, Aruga J, Rachel RA, Dolen G, Mikoshiba K, Brown S, and Mason CA (2003). Zic2 patterns binocular vision by specifying the uncrossed retinal projection. Cell 114, 545–557. 10.1016/s0092-8674(03)00684-6. [PubMed: 13678579]
53. Wang Q, Marcucci F, Cerullo I, and Mason C (2016). Ipsilateral and Contralateral Retinal Ganglion Cells Express Distinct Genes during Decussation at the Optic Chiasm. eNeuro 3, 1–28. 10.1523/ENEURO.0169-16.2016.
54. Fries M, Brown TW, Jolicoeur C, Boulan B, Boudreau-Pinsonneault C, Javed A, Abram P, and Cayouette M (2023). Pou3f1 orchestrates a gene regulatory network controlling contralateral retinogeniculate projections. Cell Rep. 42, 112985. 10.1016/j.celrep.2023.112985. [PubMed: 37590135]
55. García-Frigola C, and Herrera E (2010). Zic2 regulates the expression of Sert to modulate eye-specific refinement at the visual targets. EMBO J. 29, 3170–3183. 10.1038/emboj.2010.172. [PubMed: 20676059]
56. Saul SM, Brzezinski JA, Altschuler RA, Shore SE, Rudolph DD, Kabara LL, Halsey KE, Hufnagel RB, Zhou J, Dolan DF, and Glaser T (2008). Math5 expression and function in the central auditory system. Mol. Cell. Neurosci. 37, 153–169. 10.1016/j.mcn.2007.09.006. [PubMed: 17977745]
57. Bernstein BE, Mikkelsen TS, Xie X, Kamal M, Huebert DJ, Cuff J, Fry B, Meissner A, Wernig M, Plath K, et al. (2006). A bivalent chromatin structure marks key developmental genes in embryonic stem cells. Cell 125, 315–326. 10.1016/j.cell.2006.02.041. [PubMed: 16630819]
58. Zhang J, Roberts JM, Chang F, Schwakopf J, and Vetter ML (2023). Jarid2 promotes temporal progression of retinal progenitors via repression of Foxp1. Cell Rep. 42, 112416. 10.1016/j.celrep.2023.112416. [PubMed: 37043355]
59. Cheng L, Wong LJ, Yan N, Han RC, Yu H, Guo C, Batsuuri K, Zinzuwadia A, Guan R, Cho KS, and Chen DF (2018). Ezh2 does not mediate retinal ganglion cell homeostasis or their susceptibility to injury. PLoS One 13, e0191853. 10.1371/journal.pone.0191853. [PubMed: 29408885]
60. Wang Y, Rattner A, Zhou Y, Williams J, Smallwood PM, and Nathans J (2012). Norrin/Frizzled4 signaling in retinal vascular development and blood brain barrier plasticity. Cell 151, 1332–1344. 10.1016/j.cell.2012.10.042. [PubMed: 23217714]
61. Li H, Fredriksson L, Li X, and Eriksson U (2003). PDGF-D is a potent transforming and angiogenic growth factor. Oncogene 22, 1501–1510. 10.1038/sj.onc.1206223. [PubMed: 12629513]
62. Surace EM, Balaggan KS, Tessitore A, Mussolino C, Cotugno G, Bonetti C, Vitale A, Ali RR, and Auricchio A (2006). Inhibition of ocular neovascularization by hedgehog blockade. Mol. Ther. 13, 573–579. 10.1016/j.ymthe.2005.10.010. [PubMed: 16343995]
63. Brodie-Kommit J, Clark BS, Shi Q, Shiau F, Kim DW, Langel J, Sheely C, Ruzycki PA, Fries M, Javed A, et al. (2021). Atoh7-independent specification of retinal ganglion cell identity. Sci. Adv. 7, eabe4983. 10.1126/sciadv.abe4983. [PubMed: 33712461]
64. Laugesen A, Højfeldt JW, and Helin K (2019). Molecular Mechanisms Directing PRC2 Recruitment and H3K27 Methylation. Mol. Cell 74, 8–18. 10.1016/j.molcel.2019.03.011. [PubMed: 30951652]

65. Seo S, Richardson GA, and Kroll KL (2005). The SWI/SNF chromatin remodeling protein Brg1 is required for vertebrate neurogenesis and mediates transactivation of Ngn and NeuroD. Development 132, 105–115. 10.1242/dev.01548. [PubMed: 15576411]

66. Schweitzer J, Löhr H, Bonkowsky JL, Hübscher K, and Driever W (2013). Sim1a and Arnt2 contribute to hypothalamo-spinal axon guidance by regulating Robo2 activity via a Robo3-dependent mechanism. Development 140, 93–106. 10.1242/dev.087825. [PubMed: 23222439]

67. Hao Y, Hao S, Andersen-Nissen E, Mauck WM 3rd, Zheng S, Butler A, Lee MJ, Wilk AJ, Darby C, Zager M, et al. (2021). Integrated analysis of multimodal single-cell data. Cell 184, 3573–3587.e29. 10.1016/j.cell.2021.04.048. [PubMed: 34062119]

68. Stuart T, Srivastava A, Madad S, Lareau CA, and Satija R (2021). Single-cell chromatin state analysis with Signac. Nat. Methods 18, 1333–1341. 10.1038/s41592-021-01282-5. [PubMed: 34725479]

69. Love MI, Huber W, and Anders S (2014). Moderated estimation of fold change and dispersion for RNA-seq data with DESeq2. Genome Biol. 15, 550. 10.1186/s13059-014-0550-8. [PubMed: 25516281]

70. Li H, and Durbin R (2010). Fast and accurate long-read alignment with Burrows-Wheeler transform. Bioinformatics 26, 589–595. 10.1093/bioinformatics/btp698. [PubMed: 20080505]

71. Zhang Y, Liu T, Meyer CA, Eeckhoute J, Johnson DS, Bernstein BE, Nusbaum C, Myers RM, Brown M, Li W, and Liu XS (2008). Model-based analysis of ChIP-Seq (MACS). Genome Biol. 9, R137. 10.1186/gb-2008-9-9-r137. [PubMed: 18798982]

72. Bian F, Daghsni M, Lu F, Liu S, Gross JM, and Aldiri I (2022). Functional analysis of the Vsx2 super-enhancer uncovers distinct cis-regulatory circuits controlling Vsx2 expression during retinogenesis. Development 149, dev200642. 10.1242/dev.200642. [PubMed: 35831950]

73. Sentmanat MF, Peters ST, Florian CP, Connelly JP, and Pruett-Miller SM (2018). A Survey of Validation Strategies for CRISPR-Cas9 Editing. Sci. Rep. 8, 888. 10.1038/s41598-018-19441-8. [PubMed: 29343825]

74. Kwan KM, Fujimoto E, Grabher C, Mangum BD, Hardy ME, Campbell DS, Parant JM, Yost HJ, Kanki JP, and Chien CB (2007). The Tol2kit: a multisite gateway-based construction kit for Tol2 transposon transgenesis constructs. Dev. Dynam. 236, 3088–3099. 10.1002/dvdy.21343.

75. Huang DW, Sherman BT, and Lempicki RA (2009). Systematic and integrative analysis of large gene lists using DAVID bioinformatics resources. Nat. Protoc. 4, 44–57. 10.1038/nprot.2008.211. [PubMed: 19131956]

76. Huang DW, Sherman BT, and Lempicki RA (2009). Bioinformatics enrichment tools: paths toward the comprehensive functional analysis of large gene lists. Nucleic Acids Res. 37, 1–13. 10.1093/nar/gkn923. [PubMed: 19033363]

Highlights

- The Atoh7 *cis*-regulatory landscape is required for RGC development and optic nerve formation
- Deletion of the Atoh7 remote enhancer impacts ipsilateral RGCs and retinotectal mapping
- Loss of Atoh7 leads to derepression of the axonal guidance cue Robo3

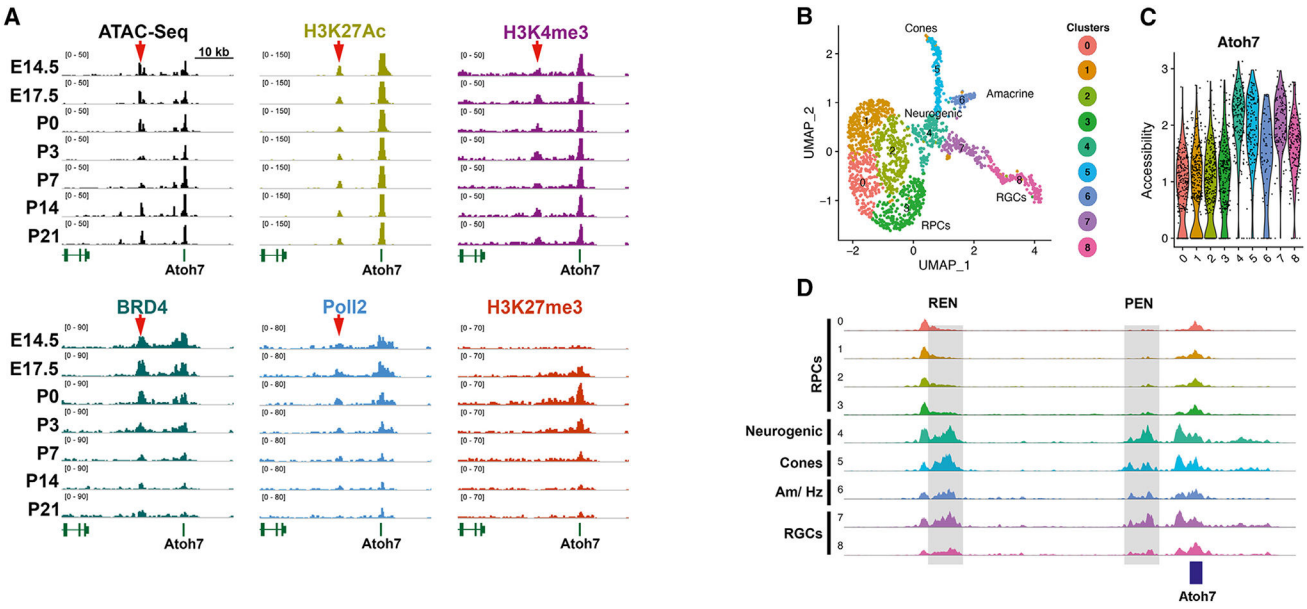

Figure 1. Enhancer landscape dynamics of the mouse Atoh7 locus during mouse retinal development

(A) Occupancy of the active enhancer marks H3K27Ac, BRD4, and RNAPII and ATAC profile near Atoh7.

(B) Uniform manifold approximation and projection (UMAP) of different clusters based on sc-ATAC-seq.

(C) Violin plot showing the distribution of chromatin accessibility of Atoh7 in retinal clusters.

(D) Coverage plots highlighting chromatin accessibility profile of Atoh7 across cell clusters. Shaded regions represent the location of the remote (REN) and proximal (PEN) enhancers.

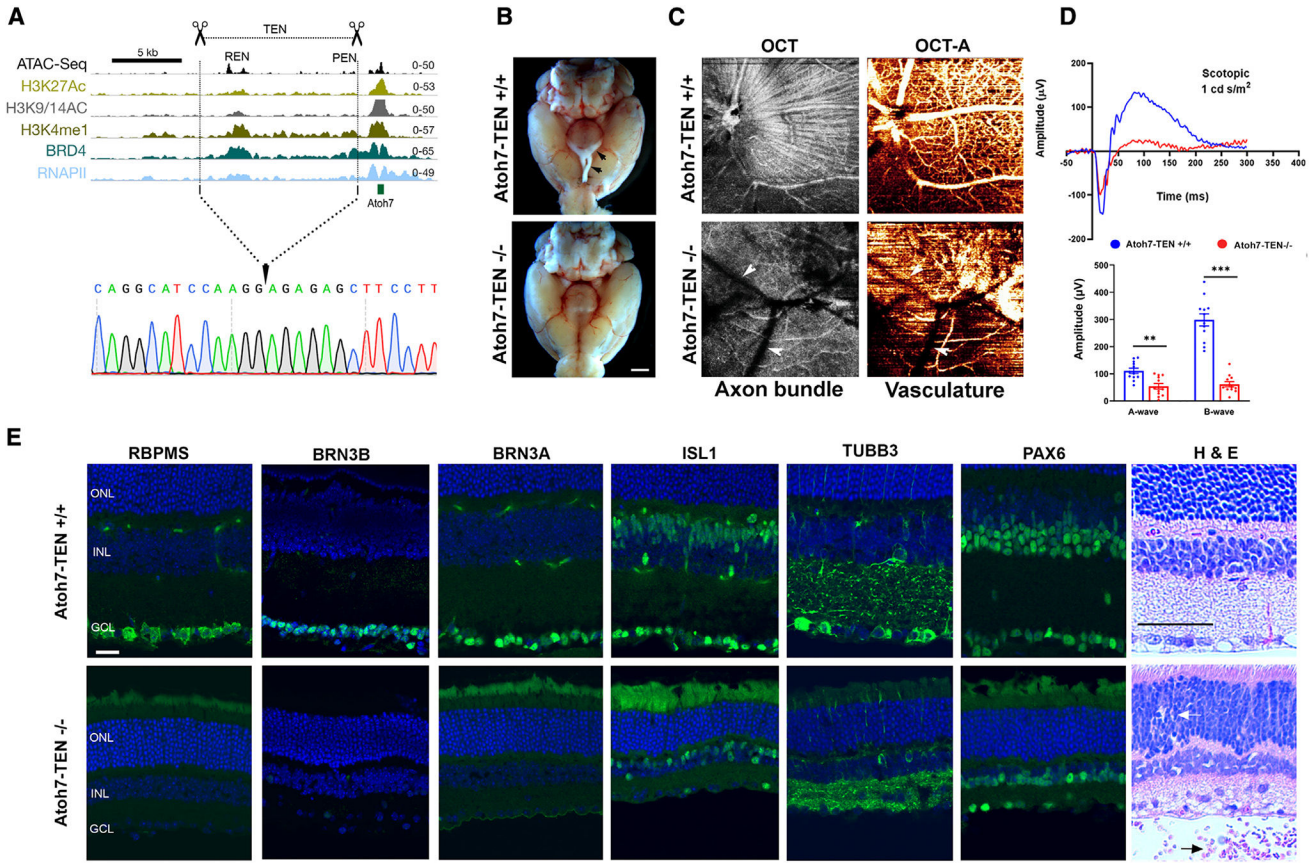

Figure 2. Structural and functional defects in the retina lacking the Atoh7 enhancer landscape (*Atoh7-TEN*$^{-/-}$)

(A) The chromatin landscape near Atoh7 in the E14.5 retina as revealed by ATAC, H3K27Ac, H3K9/14Ac, H3K4me1, BRD4, and RNAPII occupancy. The relative genomic site of the entire Atoh7 regulatory landscape and mouse knockout (KO) deletion borders (CRISPR-Cas9) are indicated by black dotted lines.

(B) Images of ventral adult brains from WT and *Atoh7-TEN*$^{-/-}$ mice showing the absence of the optic nerve and optic chiasma (indicated by black arrows in WT) in *Atoh7-TEN*$^{-/-}$ mice. Scale bar: 1 mm.

(C) Representative enface images of whole retina from adult WT and *Atoh7-TEN*$^{-/-}$ mice showing RGC axon bundle (OCT; left), and retinal blood vasculature (vis-OCT; right). White arrowheads represent the shadow of embryonic hyaloid vasculature.

(D) Representative electroretinograms (ERGs) and their quantification of adult *Atoh7-TEN*$^{-/-}$ and WT littermates recorded at a light intensity of 1 cd s/m^2 (n =6 mice for each genotype). *Atoh7-EN*$^{-/-}$ mice showed reduced amplitudes for scotopic b and a waves. n = 6 mice for each genotype (readings taken in duplicates for each animal). Data were analyzed using two-tailed Student's t test, and significance levels are shown at $^{**}p < 0.01$ and $^{***}p < 0.01$.

(E) Representative confocal images from adult WT and *Atoh7-TEN*$^{-/-}$ retinae stained for RBPMS, BRN3B, BRN3A, ISL1, TUBB3, and PAX6. Scale bar: 20 μm. H&E staining of WT and *Atoh7-TEN*$^{-/-}$ retinal sections from adult mice is also shown. Scale bar: 1 mm.

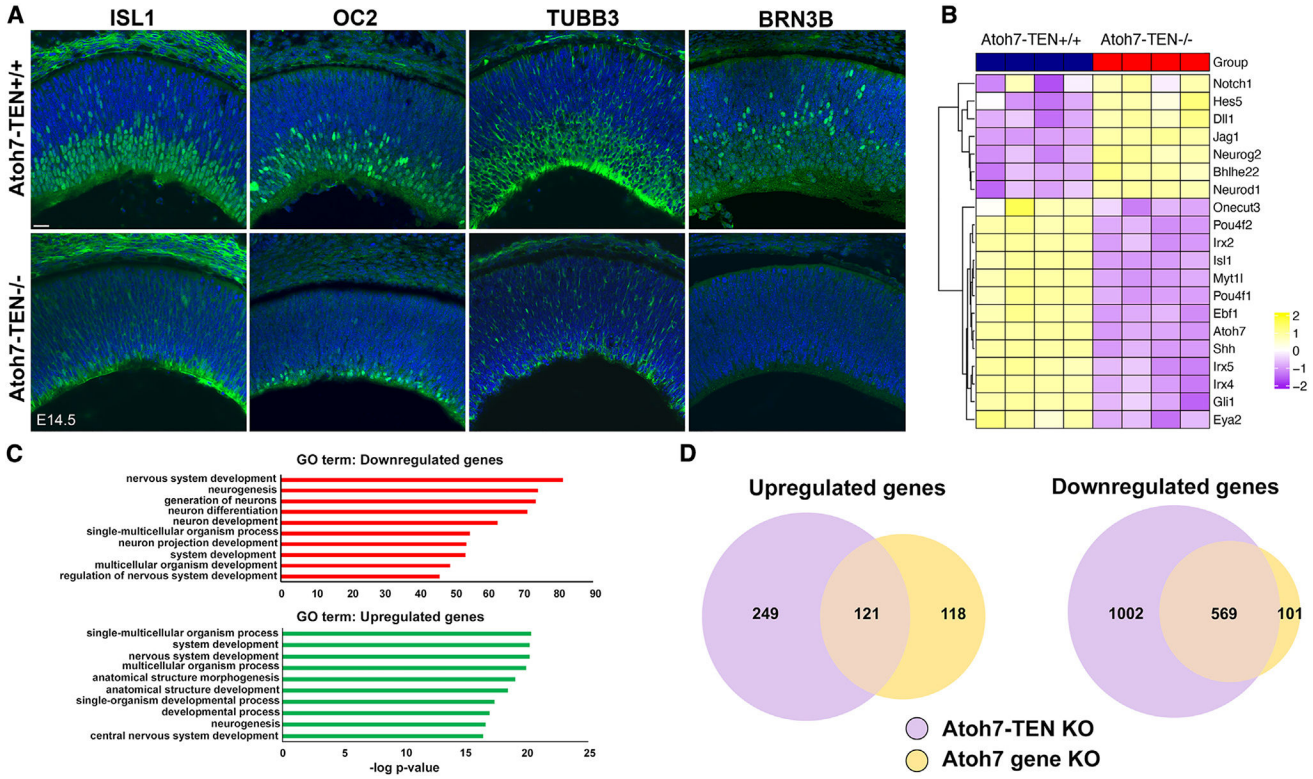

Figure 3. Loss of RGCs in Atoh7-TEN KO retina at E14.5

(A) Representative confocal images showing immunostaining of the RGC markers OC2, ISL1, and TUBB3 and BRN3B in WT and *Atoh7-TEN*$^{-/-}$ E14.5 retina. Scale bar: 20 μm.

(B) Heatmap of selected differentially expressed genes between WT and Atoh7-TEN-deficient retinae unveiled by RNA-seq analysis (n = 4 retinae per group).

(C) Gene Ontology (GO) analysis of downregulated and upregulated genes in Atoh7-TEN KO.

(D) Venn diagram showing shared differentially expressed genes in Atoh7 gene KO and Atoh7-TEN-KO retina at E14.5.

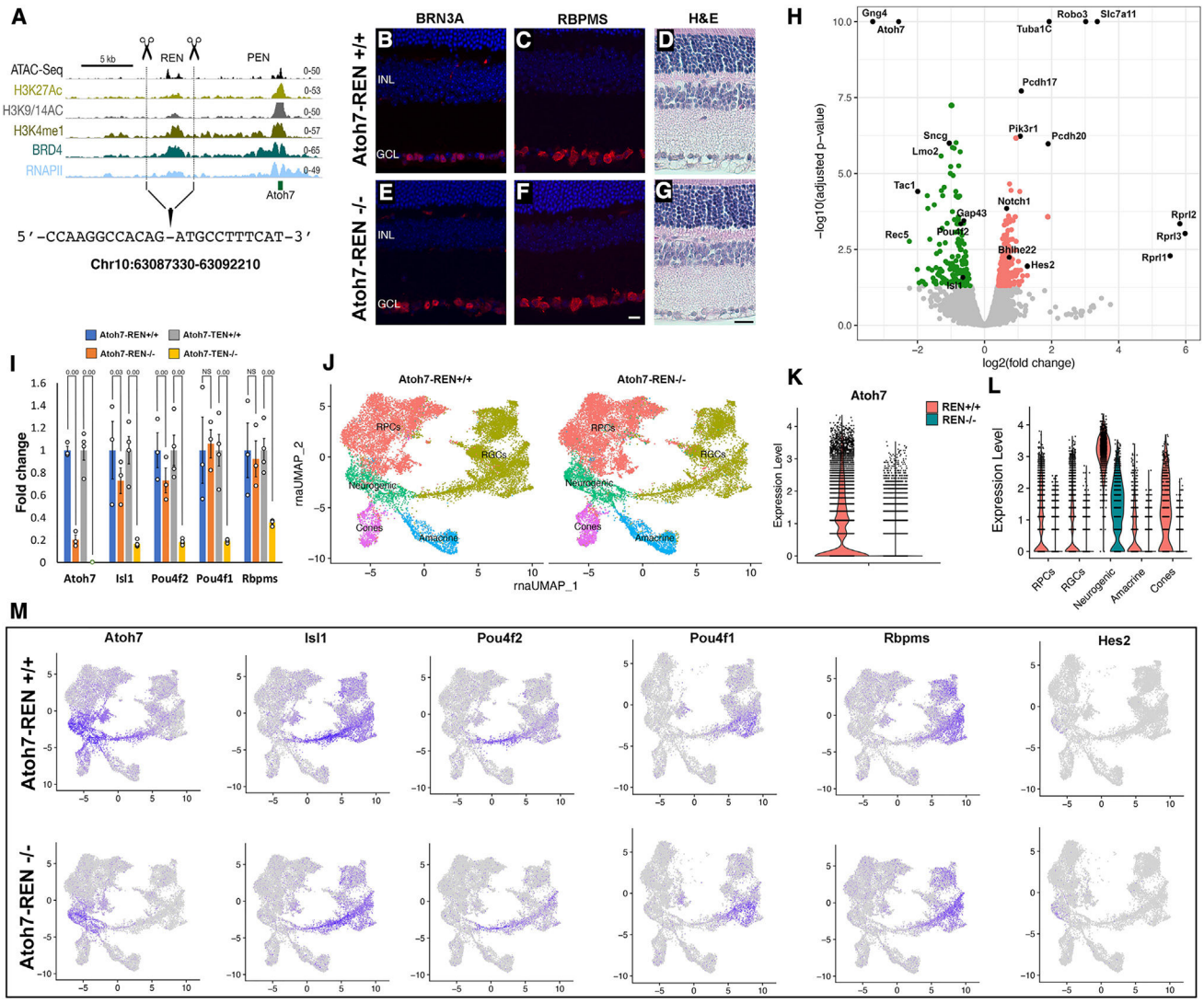

Figure 4. Transcriptomic analysis of ATOH7-REN-deficient retina at E14.5

(A) The chromatin landscape near Atoh7 in the E14.5 retina highlighting the borders of the Atoh7 remote enhancer deletion.

(B, C, E, and F) Representative confocal images of the adult retinae from *Atoh7-REN*$^{+/+}$ (top) and *Atoh7-REN*$^{-/-}$ stained with the RGC markers BRN3A and RBPMS. Scale bar: 20 μm.

(D and G) H&E staining of WT and ATOH7-REN-deficient retinae: Scale bar: 1 mm.

(H) Volcano plot from bulk RNA-seq of ATOH7-REN-KO (n = 3/genotype).

(I) Normalized RNA levels of Atoh7, Isl1, Pou4f2 (Brn3b), Pou4f1 (Brn3A), and Rbpms as revealed by RNA-seq of E14.5 retina in WT, ATOH7-REN-KO, and Atoh7-TEN-KO.

(J) UMAP plots showing retinal clusters from *Atoh7-REN*$^{+/+}$ and *Atoh7-REN*$^{-/-}$ E14.5 mice.

(K and L) Violin plots showing overall RNA levels (K) and cluster-specific expression (L) of Atoh7.

(M) RNA distribution of the indicated genes across retinal clusters in WT and ATOH7-REN-KO retina at E14.5.

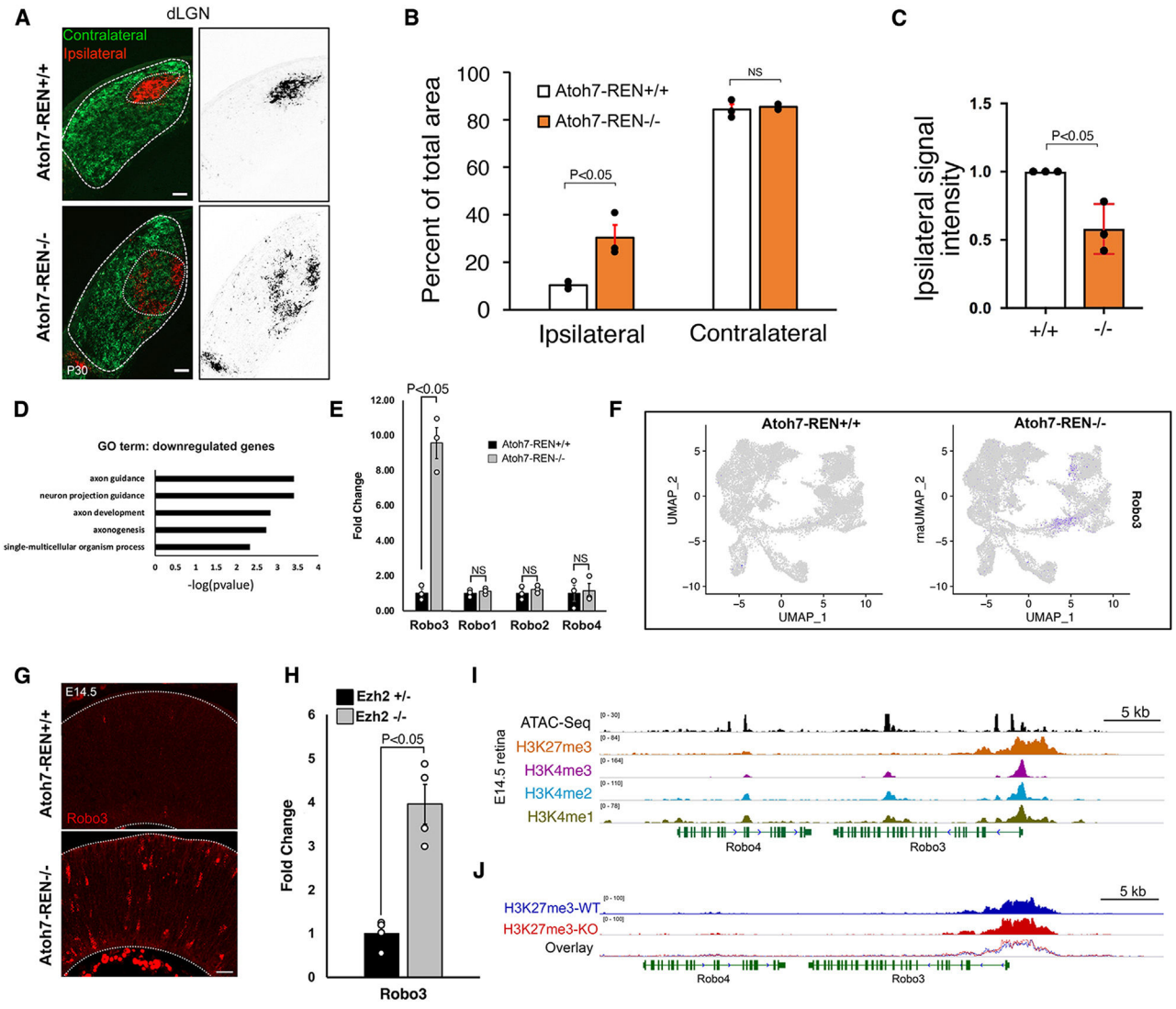

Figure 5. Atoh7 is required for proper retinotectal mapping

(A) Representative images from anterograde CTB labeling in the medial dLGN of P30 WT and *Atoh7-REN*$^{-/-}$ mice. Scale bar: 100 μm.

(B) Quantification of the service area of ipsilateral and contralateral axon innervations in *Atoh7-REN*$^{-/-}$ mice compared to WT (n = 3/genotype).

(C) Normalized signal intensity of ipsilateral projections in WT and *Atoh7-REN*$^{-/-}$ dLGN (n = 3/group). Data are compared using two tailed Student's t test ($p < 0.05$).

(D) GO term analysis of the top downregulated genes in the ATOH7-REN-deficient retinae revealed.

(E) RNA levels of Robo3 and related family members in E14.5 retina of *Atoh7-REN*$^{-/-}$ normalized to WT.

(F) UMAP distribution of Robo3 RNA in E14.5 retina from *Atoh7-REN*$^{+/+}$ and *Atoh7-REN*$^{-/-}$ mice.

(G) Confocal images of fluorescence *in situ* hybridization staining of Robo3 in E14.5 retina. Scale bar: 20 μm.

(H) Normalized RNA levels of Robo3 in Ezh2 KO retina at E16 (n = 4/genotype).[49]
(I) Chromatin profiling of the Robo3 locus at E14.5 as revealed by the histone markers H3K4me3, H3K4me2, H3K4me1, and H3K27me3.
(J) ChIP-seq tracks of H3K27me3 from WT and *Atoh7-REN*$^{-/-}$ retinae at E14.5 near Robo3.

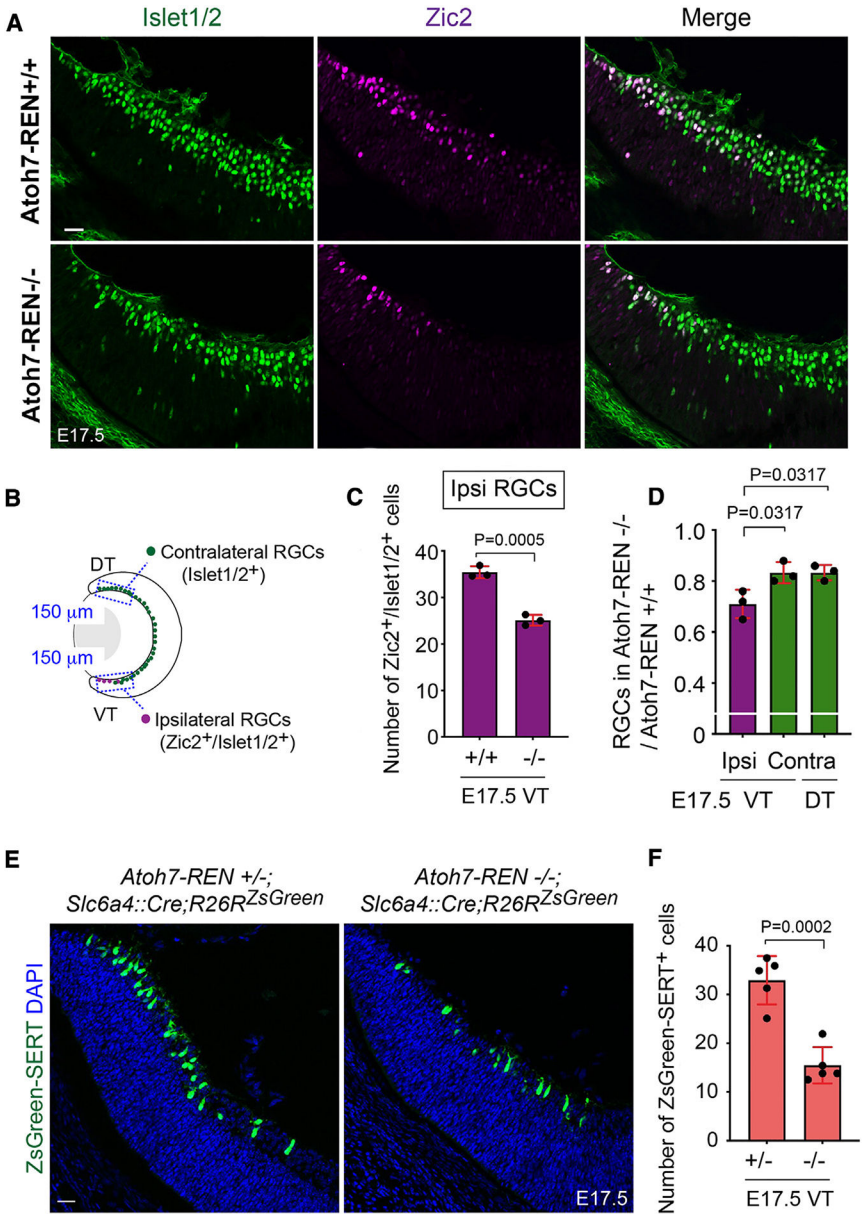

Figure 6. Atoh7 is essential for ipsilateral RGC genesis

(A) Representative confocal images from *Atoh7-REN*$^{-/-}$ and *Atoh7-REN*$^{+/+}$ E17.5 retina showing immunolabeling of Zic2 and Islet1/2 in the ventral retina. Scale bar: 20 µm.

(B) An illustration depicting the anatomical distribution of ipsilateral and contralateral RGCs in the ventral and dorsal retina. A reference area of 150 µm was considered for cell counting.

(C) Ratio of Zic2^{+}/Islet1/2^{+} cells (Ipsilateral RGCs) in *Atoh7-REN*$^{-/-}$ and *Atoh7-REN*$^{+/+}$ retinae at E17.5.

(D) Numbers of ipsilateral RGCs (Zic2^{+}/Islet1/2^{+}) in the ventral temporal (VT; D) and contralateral RGCs (Zic2^{-}, Islet1/2^{+}) in the dorsal temporal (DT; E) retina compared to the WT retina at E17.5 (n =3 embryos/genotype; 8 sections per embryo).

(E) Representative confocal images of ipRGCs as labeled with ZsGreen from control and *Atoh7-REN*$^{-/-}$*;Slc6a4::Cre;R26R*^{ZsGreen} retina at E17.5.

(F) The number of ipsilateral RGCs (ZsGreen^{+} cells) in control and *Atoh7-REN*$^{-/-}$*;Slc6a4::Cre;R26R*^{ZsGreen} (n = 5 embryos/genotype; 8 sections per embryo). All the data are presented as mean ± SD and compared using two-tailed Student's t test ($p < 0.0001$). Scale bar: 20 μm.

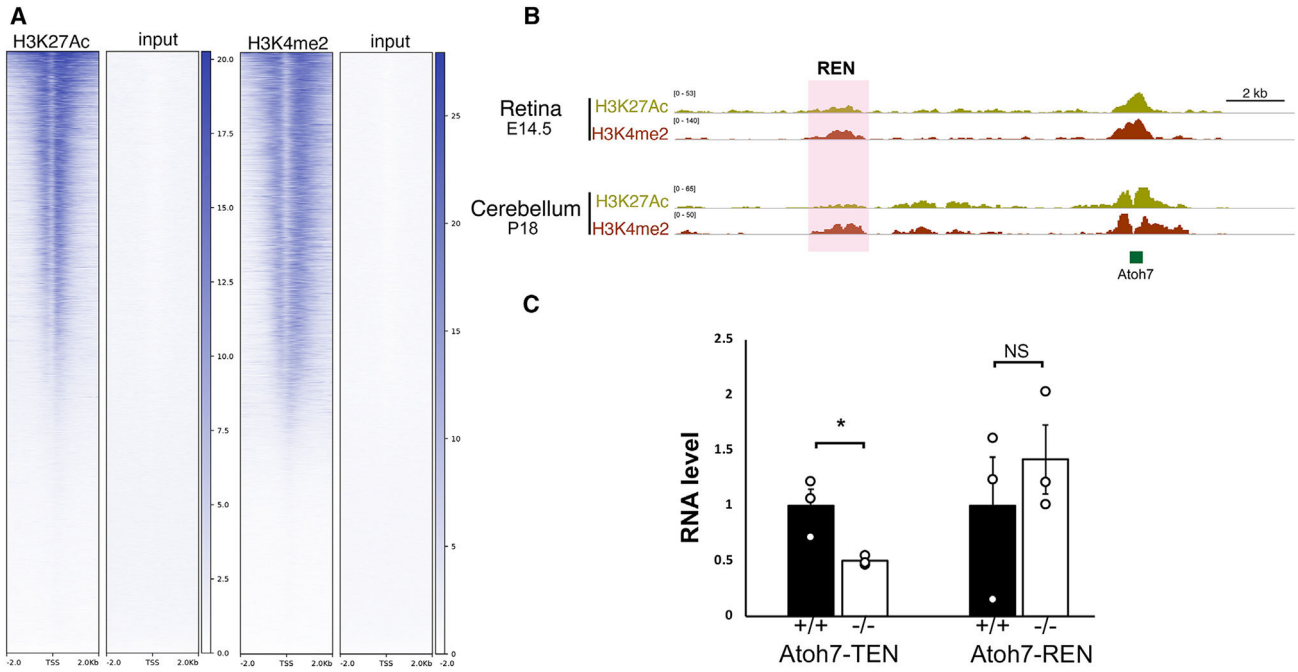

Figure 7. Requirement of Atoh7 regulatory landscape to its expression in the developing cerebellum

(A) Heatmaps of chromatin occupancy of the histone marks H3K27Ac and H3K4me2 in P18 mouse cerebellum.

(B) H3K27Ac and H3K4me2 peaks near Atoh7 in E14.5 retina and P18 cerebellum. The shaded area represents the position of the remote enhancer.

(C) Normalized RNA levels of Atoh7 in P18 cerebellum from WT, *Atoh7-REN*$^{-/-}$, and *Atoh7-TEN*$^{-/-}$ mice (n = 3/genotype, *$p \leq 0.05$).

KEY RESOURCES TABLE

REAGENT or RESOURCE	SOURCE	IDENTIFIER
Antibodies		
Mouse Anti-Isl1 & Isl2	DSHB	Cat #39.4D5-S; RRID:AB_2314683
Rabbit Anti-PAX6	Biolegend	Cat #901302; RRID:AB_2565003
Guinea pig Anti-RBPMS	PhosphoSolutions	Cat #1832; RRID:AB_2492226
Mouse Anti-BRN3A	Millipore	Cat #MAB1585; RRID:AB_94166
Mouse Anti-TUBB3 (b-III Tubulin)	Santa Cruz	Cat #Sc-80005; RRID:AB_2210816
Human Anti-ONECUT2	R&D systems	Cat #AF6294; RRID:AB_10640365
Goat Anti-BRN3B	Rockland	Cat #600-101-MJ0; RRID:AB_2942111
Rabbit Anti-Zic2	EMDMillipore	Cat #AB15392; RRID: AB 2315623
Mouse Anti-Calbindin	Sigma Aldrich	Cat #C9848; RRID:AB_476894
Mouse Anti-SOX9	Millipore	Cat #AB5535; RRID:AB_2239761
Mouse Anti-VSX2	Santa Cruz	Cat #sc-365519X; RRID:AB_10842442
Rabbit Anti-ConeA	Millipore	Cat #AB15282; RRID:AB_1163387
Lectin-PNA Pre-conjugated	Thermo Fisher Scientific	Cat #L32460; RRID:AB_3099671
CD31 (PECAM1)	Abcam	Cat #AB28364; RRID:AB_726362
Rabbit Anti-H3K27Ac	Abcam	Cat #AB4729; RRID:AB_2118291
Rabbit Anti-H3K4me2	Abcam	Cat #AB7766; RRID:AB_2560996
Rabbit Anti-H3K27me3	Millipore	Cat #07-449; RRID:AB_310624
Chemicals, peptides, and recombinant proteins		
Hoeschst 33342, trihydrochloride, trihydrate	Invitrogen	Cat #H3570
TRIReagent	Zymo Research	Cat #R2050-1-50
Critical commercial assays		
NEB Next Ultra II DNA Library Prep kit	NEB	Cat #E7645
TruChIP chromatin shearing kit	Covaris	Cat #520127
Direct-zol RNA MiniPrep kit	Zymo Research	Cat #R2050
Sc-ATAC seq Postnatal dissociation kit	MACS	Cat #130-094-802
Adult Brain Tissue Dissociation Kit	Miltenyi Biotech	Cat #130-107-677
10x Chromium Single Cell 3' v3.1 kit	10X Genomics	PN-1000128
Chromium Single Cell ATAC Reagent Kit	10X Genomics	PN-1000176
Ambion mMessage mMachine Sp6 *in vitro* transcription kit	Thermo Fisher Scientific	Cat#AM1340
Deposited data		
Sequencing data	This paper	Accession GSE245549
Experimental models: Organisms/strains		
C57BL/6J mice	Jackson Laboratory	JAX:00664
R26R^{ZsGreen} mice	Jackson Laboratory	JAX:007906

REAGENT or RESOURCE	SOURCE	IDENTIFIER
Slc6a4::*Cre* mice	Jackson Laboratory	031028-UCD
Zebrafish (Danio rerio) *vsx2*:Gal4 and *UAS*:kaede	This paper	N/A
Mouse Atoh7 enhancer knockouts	This paper	N/A
Oligonucleotides		
CRISPR gRNAs	This paper (Table S5)	N/A
Primers for genotyping Atoh7 enhancer mutants	This paper (Table S5)	N/A
Recombinant DNA		
pMErobo3b.1	Dr. Wolfgang Driever	Schweitzer et al.[66]
p3E-p2A-tdTomatoCAXX	Dr. Wolfgang Driever	Schweitzer et al.[66]
Software and algorithms		
Seurat	Hao et al.[67]	https://satijalab.org/seurat/
Signac	Stuart et al.[68]	https://stuartlab.org/signac/
Cell Ranger	10X genomics	https://support.10xgenomics.com/single-cell-multiome-atac-gex/software/pipelines/latest/what-is-cell-ranger-arc
ImageJ		https://imagej.nih.gov/ij/
Photoshop	Adobe Systems Inc., San Jose, CA, USA	
GraphPad Prism	San Diego, California USA	https://www.graphpad.com
Spilt-spectrum amplitude-decorrelation angiography (SSADA)	Piet al., 2017[31]	
DESeq2	Love et al.[69]	https://doi.org/10.1186/s13059-014-0550-8
Burrows-Wheeler Aligner (BWA) algorithm	Li and Durbin[70]	https://github.com/lh3/bwa
MACS2	Zhang et al.[71]	https://chipster.csc.fi/manual/macs2.html
R and Rstudio	CRAN	https://www.rstudio.com/
Integrated Genome Viewer	Broad Institute	https://software.broadinstitute.org/software/igv/